



**HAL**  
open science

# Homogenization of thick periodic plates: Application of the Bending-Gradient plate theory to a folded core sandwich panel

Arthur Lebée, Karam Sab

► **To cite this version:**

Arthur Lebée, Karam Sab. Homogenization of thick periodic plates: Application of the Bending-Gradient plate theory to a folded core sandwich panel. *International Journal of Solids and Structures*, 2012, 49 (19-20), pp.2778–2792. 10.1016/j.ijsolstr.2011.12.009 . hal-00794194

**HAL Id: hal-00794194**

**<https://hal.science/hal-00794194>**

Submitted on 26 Feb 2013

**HAL** is a multi-disciplinary open access archive for the deposit and dissemination of scientific research documents, whether they are published or not. The documents may come from teaching and research institutions in France or abroad, or from public or private research centers.

L'archive ouverte pluridisciplinaire **HAL**, est destinée au dépôt et à la diffusion de documents scientifiques de niveau recherche, publiés ou non, émanant des établissements d'enseignement et de recherche français ou étrangers, des laboratoires publics ou privés.

# Homogenization of thick periodic plates: application of the Bending-Gradient plate theory to a folded core sandwich panel

A. Lebé, K. Sab\*

*Université Paris-Est, Laboratoire Navier (École des Ponts ParisTech, IFSTTAR, CNRS).*

*École des Ponts ParisTech, 6 et 8 avenue Blaise Pascal.*

*77455 Marne-la-Vallée cedex2*

*tel. +33-1-64153749, fax. +33-1-64153741,*

*e-mail: arthur.lebee@enpc.fr, karam.sab@enpc.fr*

---

## Abstract

In a previous paper from the authors, the bounds from Kelsey et al. (1958) were applied to a sandwich panel including a folded core in order to estimate its shear forces stiffness (Lebé and Sab, 2010b). The main outcome was the large discrepancy of the bounds. Recently, Lebé and Sab (2011a) suggested a new plate theory for thick plates –the Bending-Gradient plate theory– which is the extension to heterogeneous plates of the well-known Reissner-Mindlin theory. In the present work, we provide the Bending-Gradient homogenization scheme and apply it to a sandwich panel including the chevron pattern. It turns out that the shear forces stiffness of the sandwich panel is strongly influenced by a skin distortion phenomenon which cannot be neglected in conventional design. Detailed analysis of this effect is provided.

*Keywords:* Plate theory, Higher-order Models, Sandwich panels, Homogenization, Periodic plates, Folded cores, Chevron pattern

---

## 1. Introduction

Sandwich panels are widespread in everyday life. Their structural efficiency is well-known and is a main criterion in possible applications. They are made of a light and thick core which is glued between two stiff skins. When the sandwich panel is bent, the skins are put into traction and compression. Thus, their design consists in maximizing their mechanical properties. This is not the case of the core which role in the sandwich panel is to resist shear forces. It must be as light as possible but not too weak. Hence the design of a core is driven by a trade-off between lightness and mechanical properties. This trade-off led to a wide diversity of cores in which cellular materials take a center stage. Among them, honeycomb structures are still considered as the most efficient cellular core geometries in many respect for high performance sandwich panels in aeronautics. However, they have some drawbacks. The iterative production process makes it an expensive material. Furthermore, once glued between skins, their cells are closed which makes them prone to store water condensation during successive take-off and landing of airplanes. This water damages the bound between core and skin and caused unexpected delaminations. Thus core design is still an innovative field nowadays. In order to tackle these drawbacks, folded cores gained new interest from the industry because of new production means and an open cell geometry.

Folded core patterns are really ancient and emerged mostly from the art of folding paper (Origami) and pleating techniques for textile (see Atelier Lognon, Paris, for instance). Therefore, the use of a periodic folded pattern as a core is well-known since the emergence of sandwich panel technology and some patents date back to the first use of honeycomb cores (Hochfeld, 1959; Rapp, 1960; Gewiss, 1960). However they remained largely ignored because of the lack of an efficient production process. Recently, continuous production means were developed (Basily and Elsayed, 2004a, 2007; Kehrle, 2004) which might create a new market for this type of core.

This regain of interest led to several studies concerning folded cores. Pattern generation was studied in details (Kling, 1997, 2005) and led to a broad variety of configurations. The present work is dedicated to the chevron pattern (Figure A.1) which is the simplest pattern and one of the first to be used as a core in sandwich panels. A large amount of experimental work was done in order to investigate the mechanical behavior of these cores. Basily and Elsayed (2004b), Nguyen et al. (2005) and Heimbs et al. (2010) mostly studied impacts on sandwich panel including folded cores. Kintscher et al. (2007) loaded folded cores with both transverse shear and compression up to failure. Fischer et al. (2009) and Baranger et al. (2010a) focused on the behavior of the aramid paper used in folded cores. Moreover, in order to spare experimental burden, intensive numerical simulations were performed by Heimbs (2009); Fischer et al. (2009) and Baranger et al. (2010b). The final objective is to implement “virtual testing” tools. These works point out the influence of the knowledge of the constitutive material as well as the critical influence of the geometrical defects on the strength of folded cores. However the core is always separated from the skins in these studies, which precludes any possible interaction between skins and core.

As already mentioned, the main action of the core is to carry shear forces. Thus, the first mechanical property one wants to assess is the shear forces stiffness of the sandwich panel and then, even more critically, the strength of the sandwich panel under shear forces. Actually, very few methods exist for such estimation because the behavior of thick plates is still a theoretical issue. The main reason is the ignorance of the effect of shear forces at microscopic scale (the unit-cell in the case of periodic sandwich panels). However, when dealing with sandwich panels, it is generally acknowledged that the skins simply put the core into transverse shear. Based on this argument, Kelsey et al. (1958) suggested bounds for estimating shear forces stiffness of sandwich panels including honeycomb. Basically, they apply uniform shear stress/strain directly to the core alone, replacing the action of the skins. In the case of chevron pattern, the upper bound was first derived by Miura (1972). Then Lebée and Sab (2010b) derived both upper and lower bounds and demonstrated that with manufactured geometries, they were very loose (more than 100% discrepancy). This gap between bounds comes from the omission of possible interaction between the skins and the core. Usually, engineers refer to the upper bound, implicitly assuming that the skins remain very stiff (Kelsey et al., 1958). However, sandwich panel theory relies on the assumption of thin skins which is an antagonistic demand. Thus we need more refined homogenization techniques in order to compute exactly the shear forces stiffness. A new theory for thick plates with varying constitutive material through the thickness was suggested in (Lebée, 2010) and (Lebée and Sab, 2011a). This theory, called Bending-Gradient theory, makes very few assumptions on the plate configuration and was successfully applied to highly anisotropic laminated plates under cylindrical bending with various material configurations (Lebée and Sab, 2011b).

The aim of this paper is to apply this new plate theory to a sandwich panel including the chevron pattern. It is organized as follows. First, in Section 2, the Bending-Gradient plate theory is summarized and the related homogenization scheme is provided. Then the sandwich panel including chevron pattern is introduced and details about implementation are given in Section 3. Results and validation with a full 3D simulation are presented in Section 4. Finally, we bring out the interaction between skins and core. The relevant parameters are identified and their influence in sandwich panel design is discussed in Section 5.

## 2. The Bending-Gradient plate model and its homogenization scheme

In this section, we first introduce the main features of the notations used in this article. Then the Bending-Gradient plate theory is summarized. Finally the extension to periodic plates is performed using energy equivalence.

### 2.1. Notations

Vectors and higher-order tensors are boldfaced and different underlinings are used for each order: vectors are straight underlined,  $\mathbf{u}$ . Second order tensors are underlined with a tilde:  $\tilde{\mathbf{M}}$  and  $\tilde{\mathbf{e}}$ . Third order tensors are underlined with a parenthesis:  $\mathbf{\Phi}$  and  $\mathbf{\Gamma}$ . Fourth order tensors are doubly underlined with a tilde:  $\tilde{\tilde{\mathbf{D}}}$  and  $\tilde{\tilde{\mathbf{c}}}$ . Sixth order tensors are doubly underlined with a parenthesis:  $\mathbf{\underline{\underline{F}}}$  and  $\mathbf{\underline{\underline{I}}}$ .

When dealing with plates, both 2-dimensional (2D) and 3D tensors are used. Thus,  $\hat{\mathbf{T}}$  denotes a 3D vector and  $\underline{\mathbf{T}}$  denotes a 2D vector or the in-plane part of  $\hat{\mathbf{T}}$ . The same notation is used for higher-order tensors:  $\hat{\boldsymbol{\sigma}}$  is the 3D second-order stress tensor while  $\underline{\boldsymbol{\sigma}}$  is its in-plane part. When dealing with tensor components, the indexes specify the dimension:  $a_{ij}$  denotes the 3D tensor  $\hat{\mathbf{a}}$  with Latin index  $i, j, k.. = 1, 2, 3$  and  $a_{\alpha\beta}$  denotes the 2D tensor  $\underline{\mathbf{a}}$  with Greek indexes  $\alpha, \beta, \gamma.. = 1, 2$ .

The transpose operation  ${}^t\bullet$  is applied to any order tensors as follows:  $({}^tA)_{\alpha\beta\dots\psi\omega} = A_{\omega\psi\dots\beta\alpha}$ . Three contraction products are defined, the usual dot product ( $\hat{\mathbf{a}} \cdot \hat{\mathbf{b}} = a_i b_i$ ), the double contraction product ( $\hat{\mathbf{a}} : \hat{\mathbf{b}} = a_{ij} b_{ji}$ ) and a triple contraction product ( $\underline{\mathbf{A}} : \underline{\mathbf{B}} = A_{\alpha\beta\gamma} B_{\gamma\beta\alpha}$ ). Einstein's notation on repeated indexes is used in these definitions. The derivation operator  $\underline{\nabla}$  is also formally represented as a vector:  $\hat{\mathbf{a}} \cdot \underline{\nabla} = a_{ij} \nabla_j = a_{ij,j}$  is the 3D divergence and  $\underline{\mathbf{a}} \otimes \underline{\nabla} = a_{\alpha\beta} \nabla_\gamma = a_{\alpha\beta,\gamma}$  is the 2D gradient. Here  $\otimes$  is the dyadic product.

## 2.2. Summary of the Bending-Gradient model (macro scale)

We consider a linear elastic plate which mid-plane is the 2D domain  $\omega \subset \mathbb{R}^2$ . Cartesian coordinates  $(x_1, x_2, x_3)$  in the reference frame  $(\hat{\mathbf{e}}_1, \hat{\mathbf{e}}_2, \hat{\mathbf{e}}_3)$  are used to describe macroscopic fields. The plate is loaded exclusively with the out-of-plane distributed force  $\hat{\mathbf{p}} = p_3 \hat{\mathbf{e}}_3$ . At this stage, the microstructure of the plate is not specified.

The membrane stress  $N_{\alpha\beta}$ , the bending moment  $M_{\alpha\beta}$ , and shear forces  $Q_\alpha$  are the usual generalized stresses for Reissner-Mindlin plates. Both  $\underline{\mathbf{N}}$  and  $\underline{\mathbf{M}}$  follows the symmetry of stress tensors:  $N_{\alpha\beta} = N_{\beta\alpha}$  and  $M_{\alpha\beta} = M_{\beta\alpha}$ . Moreover, we introduce an additional static unknown: the gradient of the bending moment  $\underline{\mathbf{R}} = \underline{\mathbf{M}} \otimes \underline{\nabla} = M_{\alpha\beta,\gamma}$ . The 2D third-order tensor  $\underline{\mathbf{R}}$  complies with the following symmetry:  $R_{\alpha\beta\gamma} = R_{\beta\alpha\gamma}$ . It is possible to derive shear forces  $\underline{\mathbf{Q}}$  from  $\underline{\mathbf{R}}$  with:  $\underline{\mathbf{Q}} = \underline{\mathbf{i}} : \underline{\mathbf{R}} \Leftrightarrow Q_\alpha = R_{\alpha\beta\beta}$ . Here  $\underline{\mathbf{i}}$  is the identity for in-plane elasticity:  $i_{\alpha\beta\gamma\delta} = \frac{1}{2} (\delta_{\alpha\gamma} \delta_{\beta\delta} + \delta_{\alpha\delta} \delta_{\beta\gamma})$ , where  $\delta_{\alpha\beta}$  is Kronecker symbol ( $\delta_{\alpha\beta} = 1$  if  $\alpha = \beta$ ,  $\delta_{\alpha\beta} = 0$  otherwise). The full bending gradient  $\underline{\mathbf{R}}$  has six components whereas  $\underline{\mathbf{Q}}$  has two components. Thus, using the full bending gradient as static unknown introduces four additional static unknowns. More precisely:  $R_{111}$  and  $R_{222}$  are respectively the cylindrical bending part of shear forces  $Q_1$  and  $Q_2$ ,  $R_{121}$  and  $R_{122}$  are respectively the torsion part of these shear forces and  $R_{112}$  and  $R_{221}$  are linked to strictly self-equilibrated stresses.

The main difference between Reissner-Mindlin and Bending-Gradient plate theories is that the Bending-Gradient plate theory enables the distinction between each component of the the gradient of the bending moment whereas they are mixed into the shear forces with Reissner-Mindlin theory. In the case of highly anisotropic laminated plates this distinction is critical for deriving good estimate of the deflection and local transverse shear distribution through the thickness (Lebée and Sab, 2011b).

Equilibrium equations and stress boundary conditions are gathered in the set of statically compatible fields:

$$\left\{ \begin{array}{l} \underline{\mathbf{N}} \cdot \underline{\nabla} = \underline{\mathbf{0}} \text{ on } \omega \\ \underline{\mathbf{M}} \otimes \underline{\nabla} - \underline{\mathbf{R}} = \underline{\mathbf{0}} \text{ on } \omega \\ (\underline{\mathbf{i}} : \underline{\mathbf{R}}) \cdot \underline{\nabla} = -p_3 \text{ on } \omega \\ \underline{\mathbf{N}} \cdot \underline{\mathbf{n}} = \underline{\mathbf{V}}^d \text{ on } \partial\omega^s \\ \underline{\mathbf{M}} = \underline{\mathbf{M}}^d \text{ on } \partial\omega^s \\ (\underline{\mathbf{i}} : \underline{\mathbf{R}}) \cdot \underline{\mathbf{n}} = V_3^d \text{ on } \partial\omega^s \end{array} \right. \quad \begin{array}{l} (1a) \\ (1b) \\ (1c) \\ (1d) \\ (1e) \\ (1f) \end{array}$$

where  $\partial\omega^s$  is the portion of edge on which static boundary conditions apply and  $\underline{\mathbf{n}}$  the related outer normal:  $\hat{\mathbf{V}}^d$  is the force per unit length and  $\underline{\mathbf{M}}^d$  the full bending moment enforced on the edge. This set of equations is almost identical to Reissner-Mindlin equations where shear forces have been replaced by the bending gradient  $\underline{\mathbf{R}}$ .

Generalized stresses  $\underline{\underline{N}}$ ,  $\underline{\underline{M}}$ , and  $\underline{\underline{R}}$  work respectively with the associated strain variables:  $\underline{\underline{e}}$ , the conventional membrane strain,  $\underline{\underline{\chi}}$  the curvature and  $\underline{\underline{\Gamma}}$  the generalized shear strain. These strain fields must comply with the following compatibility conditions and boundary conditions:

$$\begin{cases} \underline{\underline{e}} = \underline{\underline{i}} : (\underline{\nabla} \otimes \underline{\underline{U}}) & \text{on } \omega & (2a) \\ \underline{\underline{\chi}} = \underline{\underline{\Phi}} \cdot \underline{\nabla} & \text{on } \omega & (2b) \\ \underline{\underline{\Gamma}} = \underline{\underline{\Phi}} + \underline{\underline{i}} \cdot \underline{\nabla} U_3 & \text{on } \omega & (2c) \\ \underline{\underline{\Phi}} \cdot \underline{\underline{n}} = \underline{\underline{H}}^d & \text{on } \partial\omega^k & (2d) \\ \underline{\underline{U}} = \underline{\underline{U}}^d & \text{on } \partial\omega^k & (2e) \end{cases}$$

where  $\underline{\underline{U}}$  is the average through the thickness of the plate 3D displacement and  $\underline{\underline{\Phi}}$  is the generalized rotation.  $\underline{\underline{\Gamma}}$  and  $\underline{\underline{\Phi}}$  are 2D-third-order tensors with the following symmetry:  $\Phi_{\alpha\beta\gamma} = \Phi_{\beta\alpha\gamma}$ . Moreover,  $\partial\omega^k$  is the portion of edge on which kinematic boundary conditions apply:  $\underline{\underline{U}}^d$  is a given displacement and  $\underline{\underline{H}}^d$  is a symmetric second-order tensor related to a forced rotation on the edge. These fields are almost identical to Reissner-Mindlin kinematically compatible fields where the rotation pseudo-vector is replaced by the generalized rotation  $\underline{\underline{\Phi}}$ . Assuming  $\underline{\underline{\Phi}} = \underline{\underline{i}} \cdot \underline{\underline{\varphi}}$  in (2) leads to a Reissner-Mindlin-like kinematic.

Finally, assuming uncoupling between  $\underline{\underline{R}}$  and  $(\underline{\underline{N}}, \underline{\underline{M}})$  (see Section 2.4.3) the Bending-Gradient plate constitutive equations are written as:

$$\begin{cases} \underline{\underline{N}} = \underline{\underline{A}} : \underline{\underline{e}} + \underline{\underline{B}} : \underline{\underline{\chi}} & (3a) \\ \underline{\underline{M}} = {}^t \underline{\underline{B}} : \underline{\underline{e}} + \underline{\underline{D}} : \underline{\underline{\chi}} & (3b) \\ \underline{\underline{\Gamma}} = \underline{\underline{f}} : \underline{\underline{R}}, \quad \text{and} \quad (\underline{\underline{I}} - \underline{\underline{f}} : \underline{\underline{F}}) : \underline{\underline{\Gamma}} = 0 & (3c) \end{cases}$$

where  $(\underline{\underline{A}}, \underline{\underline{B}}, \underline{\underline{D}})$  are conventional Kirchhoff-Love stiffness tensors and the generalized shear compliance tensor  $\underline{\underline{f}}$  is a sixth order tensor<sup>1</sup>. Since  $\underline{\underline{f}}$  is not always invertible, Moore-Penrose pseudo inverse for the shear stiffness tensor  $\underline{\underline{F}}$  is introduced:

$$\underline{\underline{F}} = \lim_{\kappa \rightarrow 0} \left( \underline{\underline{f}} : \underline{\underline{f}} + \kappa \underline{\underline{I}} \right)^{-1} : \underline{\underline{f}}$$

where  $\underline{\underline{I}}$  is the identity for 2D sixth-order tensors following the generalized shear compliance  $\underline{\underline{f}}$  minor and major symmetries ( $I_{\alpha\beta\gamma\delta\epsilon\zeta} = i_{\alpha\beta\epsilon\zeta} \delta_{\gamma\delta}$ ). Hence, the second part of Equation 3c enforce kinematic constraints when  $\underline{\underline{f}}$  is not definite.

The solution of the plate model must comply with the three sets of equations (1, 2, 3). The compliance  $\underline{\underline{f}}$  is positive. However when  $\underline{\underline{f}}$  is not definite, there is a set of solutions, up to a self-stress field.

The stiffness tensors  $\underline{\underline{A}}$ ,  $\underline{\underline{B}}$ ,  $\underline{\underline{D}}$  and  $\underline{\underline{f}}$  are derived using the homogenization scheme which will be discussed later on. Then, the stress energy density is defined as:

$$w^{*BG}(\underline{\underline{N}}, \underline{\underline{M}}, \underline{\underline{R}}) = \frac{1}{2} \left( \underline{\underline{N}} : \underline{\underline{a}} : \underline{\underline{N}} + 2 \underline{\underline{N}} : \underline{\underline{b}} : \underline{\underline{M}} + \underline{\underline{M}} : \underline{\underline{d}} : \underline{\underline{M}} + {}^t \underline{\underline{R}} : \underline{\underline{f}} : \underline{\underline{R}} \right) \quad (4)$$

where  $(\underline{\underline{a}}, \underline{\underline{b}}, \underline{\underline{d}})$  are the Kirchhoff-Love compliance tensors (reciprocal of  $(\underline{\underline{A}}, \underline{\underline{B}}, \underline{\underline{D}})$ ).

<sup>1</sup> $f_{\alpha\beta\gamma\delta\epsilon\zeta}$  follows major symmetry:  $f_{\alpha\beta\gamma\delta\epsilon\zeta} = f_{\zeta\epsilon\delta\gamma\beta\alpha}$  and minor symmetry  $f_{\alpha\beta\gamma\delta\epsilon\zeta} = f_{\beta\alpha\gamma\delta\epsilon\zeta}$ . Thus there are only 21 independent components.

### 2.3. Distance between the Reissner-Mindlin and the Bending-Gradient model

In some cases, the Bending-Gradient is turned into a Reissner-Mindlin plate model. This is the case for homogeneous plates. In order to estimate the difference between both plate models we defined the isotropic projection of the Bending-Gradient stress energy density on the Reissner-Mindlin one in (Lebée and Sab, 2011a).

According to this projection, the Reissner-Mindlin part of  $\underline{\underline{f}}$  is:

$$\underline{\underline{f}}^{RM} = \left( \frac{2}{3} \underline{\underline{i}} \cdot \underline{\underline{i}} \right) \cdot \underline{\underline{f}} \cdot \left( \frac{2}{3} \underline{\underline{i}} \cdot \underline{\underline{i}} \right) \quad (5)$$

where  $\underline{\underline{f}}^{RM}$  can be considered as the restriction of  $\underline{\underline{f}}$  when setting warping unknowns to zero. Consequently, we introduce the pure warping part of  $\underline{\underline{f}}$  as the orthogonal complement of  $\underline{\underline{f}}^{RM}$ :

$$\underline{\underline{f}}^W = \underline{\underline{f}} - \underline{\underline{f}}^{RM} \quad (6)$$

Finally we suggested the following relative distance between the Bending-Gradient and the Reissner-Mindlin stress energy densities:

$$\Delta^{RM/BG} = \frac{\|\underline{\underline{f}}^W\|}{\|\underline{\underline{f}}\|}, \quad \text{where} \quad \|\underline{\underline{f}}\| = \sqrt{f_{\alpha\beta\gamma\delta\epsilon\zeta} f_{\alpha\beta\gamma\delta\epsilon\zeta}} \quad (7)$$

$\Delta^{RM/BG}$  gives an estimate of the pure warping fraction of the shear stress energy and is a criterion for assessing the need of the Bending-Gradient model:  $0 \leq \Delta^{RM/BG} < 1$ . When the plate constitutive equation reduces to a Reissner-Mindlin one, we have exactly  $\Delta^{RM/BG} = 0$  and both theories are strictly identical.

### 2.4. Homogenization scheme (micro scale)

Let us consider a plate generated by periodicity of a unit-cell  $Y$  according to the in-plane Directions 1 and 2 (Figure A.2). The upper face  $\partial Y_3^+$  and the lower face  $\partial Y_3^-$  are traction free and the lateral faces  $\partial Y_l$  must fulfill periodicity conditions.  $A_Y$  is the area of the unit-cell cross section with the plate mid-plane.  $\underline{\underline{y}} = (y_1, y_2, y_3)$  is the set of coordinates in the unit-cell reference frame.

Exactly as Cecchi and Sab (2007) did for Reissner-Mindlin homogenization of periodic plates, it is possible to extend the Bending-Gradient plate theory to periodic plates. For this, it is implicitly assumed that macroscopic fields  $(\underline{\underline{N}}, \underline{\underline{M}}, \underline{\underline{R}})$  and their associated stress energy density vary slowly with respect to the size of the unit-cell. This is very conventional in homogenization. Then, using Hill-Mandel principle, the average of the local energy in the unit-cell (microscopic energy) is assumed equal to the plate energy (macroscopic energy). For stress energy density this is equivalent to setting:

$$w^{*BG}(\underline{\underline{N}}, \underline{\underline{M}}, \underline{\underline{R}}) = \frac{1}{2} \left\langle \hat{\underline{\underline{\sigma}}}^{BG}(\underline{\underline{y}}) : \hat{\underline{\underline{S}}}(\underline{\underline{y}}) : \hat{\underline{\underline{\sigma}}}^{BG}(\underline{\underline{y}}) \right\rangle \quad (8)$$

where

$$\langle f \rangle = \frac{1}{A_Y} \int_Y f(\underline{\underline{y}}) dY \quad (9)$$

is the normalized average (surface average) on the unit-cell,  $\hat{\underline{\underline{S}}}$  is the 3D compliance tensor and  $\hat{\underline{\underline{\sigma}}}^{BG}$  is an approximation of the local stress field in the unit-cell generated by the macroscopic static unknowns  $(\underline{\underline{N}}, \underline{\underline{M}}, \underline{\underline{R}})$ . More precisely, the field localization  $\hat{\underline{\underline{\sigma}}}^{BG}$  is a linear application from  $(\underline{\underline{N}}, \underline{\underline{M}}, \underline{\underline{R}})$  to a 3D stress field in the unit-cell which is detailed as follows:

$$\hat{\underline{\underline{\sigma}}}^{BG}(\underline{\underline{y}}) = \hat{\underline{\underline{\sigma}}}^{(N)}(\underline{\underline{y}}) + \hat{\underline{\underline{\sigma}}}^{(M)}(\underline{\underline{y}}) + \hat{\underline{\underline{\sigma}}}^{(R)}(\underline{\underline{y}})$$

where  $\hat{\boldsymbol{\sigma}}^{(N)}$ ,  $\hat{\boldsymbol{\sigma}}^{(M)}$ , and  $\hat{\boldsymbol{\sigma}}^{(R)}$  are 3D stress fields generated respectively by  $\underline{\mathbf{N}}$ ,  $\underline{\mathbf{M}}$  and  $\underline{\mathbf{R}}$ :

$$\begin{cases} \sigma_{ij}^{(N)} = s_{ij\alpha\beta}^{(N)}(\hat{\mathbf{y}})N_{\beta\alpha} & (10a) \\ \sigma_{ij}^{(M)} = s_{ij\alpha\beta}^{(M)}(\hat{\mathbf{y}})M_{\beta\alpha} & (10b) \\ \sigma_{ij}^{(R)} = s_{ij\alpha\beta\gamma}^{(R)}(\hat{\mathbf{y}})R_{\gamma\beta\alpha} & (10c) \end{cases}$$

where  $s_{ij\alpha\beta}^{(N)}(\hat{\mathbf{y}})$ ,  $s_{ij\alpha\beta}^{(M)}(\hat{\mathbf{y}})$  and  $s_{ij\alpha\beta\gamma}^{(R)}(\hat{\mathbf{y}})$  are localization field tensors (unit load fields). This can be rewritten using contraction products as:

$$\hat{\boldsymbol{\sigma}}^{BG} = \hat{\underline{\underline{\mathbf{s}}}}^{(N)} : \underline{\mathbf{N}} + \hat{\underline{\underline{\mathbf{s}}}}^{(M)} : \underline{\mathbf{M}} + \hat{\underline{\underline{\mathbf{s}}}}^{(R)} : \underline{\mathbf{R}}$$

When dealing with laminated plates it is possible to derive localization fields  $\hat{\underline{\underline{\mathbf{s}}}}^{(N)}$ ,  $\hat{\underline{\underline{\mathbf{s}}}}^{(M)}$  and  $\hat{\underline{\underline{\mathbf{s}}}}^{(R)}$  explicitly from the constitutive material behavior (Lebée and Sab, 2011a). However, this is not possible with periodic plates in the general case and deriving localization fields necessitates the resolution of auxiliary problems. First, the Kirchhoff-Love auxiliary problem was suggested by Caillerie (1984) and enables the derivation of the effective Kirchhoff-Love membrane and flexural moduli of the periodic plate  $\underline{\underline{\mathbf{A}}}$ ,  $\underline{\underline{\mathbf{B}}}$  and  $\underline{\underline{\mathbf{D}}}$ , as well as the local 3D stresses  $\hat{\underline{\underline{\mathbf{s}}}}^{(e)}(\hat{\mathbf{y}})$  and  $\hat{\underline{\underline{\mathbf{s}}}}^{(\chi)}(\hat{\mathbf{y}})$  related to the membrane strain and the curvature. Then a new generalized shear auxiliary problem is introduced in this paper, using Kirchhoff-Love localization fields as loading inputs, in order to derive the generalized shear compliance  $\underline{\underline{\mathbf{f}}}$  and the related localization stress field  $\hat{\underline{\underline{\mathbf{s}}}}^{(R)}(\hat{\mathbf{y}})$ .

#### 2.4.1. Kirchhoff-Love auxiliary problem

Kirchhoff-Love homogenization of periodic plates was first proposed by Caillerie (1984) and followed by Kohn and Vogelius (1984). The auxiliary problem is stated as follows:

$$\mathcal{P}^{LK} \begin{cases} \hat{\boldsymbol{\sigma}}^{KL} \cdot \hat{\nabla} = 0 & (11a) \\ \hat{\boldsymbol{\sigma}}^{KL} = \hat{\underline{\underline{\mathbf{C}}}}(\hat{\mathbf{y}}) : \hat{\boldsymbol{\varepsilon}}^{KL} & (11b) \\ \hat{\boldsymbol{\varepsilon}}^{KL} = \hat{\boldsymbol{\varepsilon}} + y_3 \hat{\boldsymbol{\chi}} + \hat{\nabla} \otimes^s \hat{\mathbf{u}}^{per} & (11c) \\ \hat{\boldsymbol{\sigma}} \cdot \hat{\mathbf{e}}_3 = 0 \text{ on free faces } \partial Y_3^\pm & (11d) \\ \hat{\boldsymbol{\sigma}} \cdot \hat{\mathbf{n}} \text{ skew-periodic on lateral boundaries } \partial Y_l & (11e) \\ \hat{\mathbf{u}}^{per}(y_1, y_2, y_3) \text{ } (y_1, y_2)\text{-periodic on lateral boundaries } \partial Y_l & (11f) \end{cases}$$

Basically it enforces the membrane strains  $\boldsymbol{\varepsilon}$  and the curvatures  $\boldsymbol{\chi}$  on average on the unit-cell while taking into account periodicity in the  $(x_1, x_2)$ -plane and traction-free conditions on the upper and lower faces of the plate. In Equation 11c,  $\hat{\boldsymbol{\varepsilon}}$  and  $\hat{\boldsymbol{\chi}}$  denote the out-of-plane extension of the in-plane tensors  $\boldsymbol{\varepsilon}$  and  $\boldsymbol{\chi}$ :

$$\hat{\boldsymbol{\varepsilon}} = \begin{pmatrix} e_{11} & e_{12} & 0 \\ e_{21} & e_{22} & 0 \\ 0 & 0 & 0 \end{pmatrix} \quad \text{and} \quad \hat{\boldsymbol{\chi}} = \begin{pmatrix} \chi_{11} & \chi_{12} & 0 \\ \chi_{21} & \chi_{22} & 0 \\ 0 & 0 & 0 \end{pmatrix} \quad (12)$$

Solving the problem for each individual component of  $\boldsymbol{\varepsilon}$  and  $\boldsymbol{\chi}$  leads to the localization stress fields  $\hat{\underline{\underline{\mathbf{s}}}}^{(e)}$  and  $\hat{\underline{\underline{\mathbf{s}}}}^{(\chi)}$ . Kirchhoff-Love plate moduli are then evaluated as follows:

$$\underline{\underline{\mathbf{A}}} = \left\langle {}^t \hat{\underline{\underline{\mathbf{s}}}}^{(e)} : \hat{\underline{\underline{\mathbf{S}}}} : \hat{\underline{\underline{\mathbf{s}}}}^{(e)} \right\rangle, \quad \underline{\underline{\mathbf{B}}} = \left\langle {}^t \hat{\underline{\underline{\mathbf{s}}}}^{(e)} : \hat{\underline{\underline{\mathbf{S}}}} : \hat{\underline{\underline{\mathbf{s}}}}^{(\chi)} \right\rangle, \quad \underline{\underline{\mathbf{D}}} = \left\langle {}^t \hat{\underline{\underline{\mathbf{s}}}}^{(\chi)} : \hat{\underline{\underline{\mathbf{S}}}} : \hat{\underline{\underline{\mathbf{s}}}}^{(\chi)} \right\rangle \quad (13)$$

Finally, using the inverted Kirchhoff-Love plate constitutive law,

$$\boldsymbol{\varepsilon} = \underline{\underline{\mathbf{a}}} : \underline{\mathbf{N}} + \underline{\underline{\mathbf{b}}} : \underline{\mathbf{M}}, \quad \boldsymbol{\chi} = {}^t \underline{\underline{\mathbf{b}}} : \underline{\mathbf{N}} + \underline{\underline{\mathbf{d}}} : \underline{\mathbf{M}} \quad (14)$$

and localization tensors  $\hat{\underline{\underline{s}}}^{(e)}$  and  $\hat{\underline{\underline{s}}}^{(x)}$ , it is possible to write the local stress field generated by membrane stress and bending moment as:

$$\hat{\underline{\underline{\sigma}}}^{(N)} = \hat{\underline{\underline{s}}}^{(N)} : \underline{\underline{N}} = \left( \hat{\underline{\underline{s}}}^{(e)} : \underline{\underline{a}} + \hat{\underline{\underline{s}}}^{(x)} : \underline{\underline{t}} \underline{\underline{b}} \right) : \underline{\underline{N}} \quad \text{and} \quad \hat{\underline{\underline{\sigma}}}^{(M)} = \hat{\underline{\underline{s}}}^{(M)} : \underline{\underline{M}} = \left( \hat{\underline{\underline{s}}}^{(e)} : \underline{\underline{b}} + \hat{\underline{\underline{s}}}^{(x)} : \underline{\underline{d}} \right) : \underline{\underline{M}} \quad (15)$$

#### 2.4.2. The generalized shear auxiliary problem

Exactly as for laminated plates (Lebée and Sab, 2011a), it is possible to bring out a volume force related to  $\underline{\underline{R}}$  when assuming a linear variation of the bending moment in the  $(y_1, y_2)$ -plane:  $\underline{\underline{M}} = \underline{\underline{R}} \cdot \underline{\underline{y}}$ . Inserting this in the localization equation (15) and taking the 3D divergence of the stress  $\hat{\underline{\underline{\sigma}}}^{(M)}$ , leads to the body force in the unit-cell generated by a uniform gradient of the bending moment,  $\underline{\underline{R}}$ :

$$f_i^{(R)} = \left( s_{ij\beta\alpha}^{(M)}(\underline{\underline{y}}) R_{\alpha\beta\gamma} y_\gamma \right) \nabla_j = s_{i\gamma\beta\alpha}^{(M)}(\underline{\underline{y}}) R_{\alpha\beta\gamma} \quad (16)$$

Then the Bending-Gradient 3D stress  $\hat{\underline{\underline{\sigma}}}^{(R)}$  is defined as the stress field which equilibrates  $\underline{\underline{f}}^{(R)}$ . Accordingly, the generalized shear auxiliary problem on the unit-cell is defined as:

$$\mathcal{P}^{BG} \begin{cases} \hat{\underline{\underline{\sigma}}}^{(R)} \cdot \hat{\underline{\underline{\nabla}}} + \underline{\underline{f}}^{(R)}(\underline{\underline{y}}) = 0 & (17a) \\ \hat{\underline{\underline{\sigma}}}^{(R)} = \hat{\underline{\underline{C}}}(\underline{\underline{y}}) : \left( \hat{\underline{\underline{\nabla}}} \otimes^s \underline{\underline{u}}^{(R)} \right) & (17b) \\ \hat{\underline{\underline{\sigma}}}^{(R)} \cdot \underline{\underline{e}}_3 = 0 \text{ on free faces } \partial Y_3^\pm & (17c) \\ \hat{\underline{\underline{\sigma}}}^{(R)} \cdot \underline{\underline{n}} \text{ skew-periodic on lateral boundaries } \partial Y_l & (17d) \\ \underline{\underline{u}}^{(R)}(y_1, y_2, y_3) \text{ } (y_1, y_2)\text{-periodic on lateral boundaries } \partial Y_l & (17e) \end{cases}$$

Solving  $\mathcal{P}^{BG}$  for each component of  $\underline{\underline{R}}$  leads to the localization stress field  $s_{ij\alpha\beta\gamma}^{(R)}$  associated to  $\underline{\underline{R}}$ . The overall stress is obtained by linear combination:

$$\hat{\underline{\underline{\sigma}}}^{(R)} = \hat{\underline{\underline{s}}}^{(R)}(\underline{\underline{y}}) : \underline{\underline{R}} \quad (18)$$

It is then possible to identify the Bending-Gradient compliance tensor as:

$$\underline{\underline{f}} = \left\langle^t \left( \hat{\underline{\underline{s}}}^{(R)} \right) : \hat{\underline{\underline{S}}}(\underline{\underline{y}}) : \hat{\underline{\underline{s}}}^{(R)} \right\rangle \quad (19)$$

Contrary to axiomatic approaches, the main asset of this homogenization scheme is that no assumption is made on the strain or stress related to shear forces. Actually, the effect of  $\underline{\underline{R}}$  on the local stress distribution is introduced through the body force  $\underline{\underline{f}}^{(R)}$  which cannot be chosen *a priori* but derives from the bending moment localization field.

#### 2.4.3. Effect of symmetries of the unit-cell on the constitutive equation

There are  $3 + 3 + 6 = 12$  static unknowns. Thus *a priori* 78 independent moduli should be derived for the constitutive equations. However, when the unit-cell follows some invariance through an orthogonal transformation, uncouplings occurs. In Lebée and Sab (2011a) a symmetry index was introduced. It is positive when a generalized stress component is symmetric with respect to the transformation and negative when a generalized stress component is skew symmetric. Two generalized stress components are uncoupled when they have opposite symmetry indices for a given transformation.

Table 1 gives this index for three possible invariances of the unit-cell. When the unit-cell is unchanged through a  $\pi$  angle rotation of a vertical axis (invariance  $\mathcal{S}$ ), then the Kirchhoff-Love stresses ( $\underline{\underline{N}}, \underline{\underline{M}}$ ) are uncoupled from  $\underline{\underline{R}}$ . When the unit-cell follows the mirror symmetry with respect to the mid-plane (invariance  $\mathcal{M}$ ), then membrane stress are uncoupled from bending moments. Finally, the plate is orthotropic when the unit-cell is invariant through a vertical plane symmetry (invariance  $\mathcal{O}$ ). When all these symmetries occurs, their remain 4 moduli for membrane stress, 4 moduli for bending moments and 12 moduli for the bending gradient (further simplifications can be found in (Lebée and Sab, 2011b)).

	$N_{11}$	$N_{22}$	$N_{12}$	$M_{11}$	$M_{22}$	$M_{12}$	$R_{111}$	$R_{221}$	$R_{121}$	$R_{112}$	$R_{222}$	$R_{122}$
$\mathcal{S}$ $\begin{pmatrix} -1 & 0 & 0 \\ 0 & -1 & 0 \\ 0 & 0 & 1 \end{pmatrix}$	+	+	+	+	+	+	-	-	-	-	-	-
$\mathcal{M}$ $\begin{pmatrix} 1 & 0 & 0 \\ 0 & 1 & 0 \\ 0 & 0 & -1 \end{pmatrix}$	+	+	+	-	-	-	-	-	-	-	-	-
$\mathcal{O}$ $\begin{pmatrix} 1 & 0 & 0 \\ 0 & -1 & 0 \\ 0 & 0 & 1 \end{pmatrix}$	+	+	-	+	+	-	+	+	-	-	-	+

Table 1: Symmetry index and generalized stress components for three main invariances of the unit-cell

### 3. Application to a sandwich panel including the chevron pattern

#### 3.1. Description of the sandwich panel including the folded core

In this work, we consider a sandwich panel fully made of aluminum sheets with  $E_m = 73 \text{ GPa}$  and  $\nu_m = 0.3$ . The chevron pattern core is welded between an upper and a lower skin and we assume a perfect geometry. The skins thickness is  $t_s$  and the core's facets thickness is  $t_f$ . Regarding the core, the investigated geometric parameters are similar to Nguyen et al. (2005) and the same as in Lebée and Sab (2010b). Figure A.3 gives the definition of the only four parameters necessary to set the core configuration and shows the core for several shape ratios  $a_0/b_0$ . Three parameters are fixed in the present study:  $a_0 = 30 \text{ mm}$ ,  $\delta = 72.2^\circ$ ,  $\alpha = 14.9^\circ$ . The core thickness is then:  $t_c = a_0 \sin \delta = 28.5 \text{ mm}$ . Varying  $b_0 \in [20 \text{ mm}, 60 \text{ mm}]$  as in Lebée and Sab (2010b) enables the investigation of the facets shape ratio.

Finally we suggest the following range for the facet thickness:  $t_f \in [0.02 \text{ mm}, 0.5 \text{ mm}]$  and for the skin thickness:  $t_s \in [0.1 \text{ mm}, 5 \text{ mm}]$ . The facet thickness range is a bit wider than producible thicknesses and the skins thickness range is rather wide. This leads to a very wide range for the contrast ratio  $t_s/t_f$  and will provide a comprehensive view of its influence on the sandwich panel overall behavior. Let us just remind the reader of that having  $t_s/t_f > 100$  is not interesting in sandwich panel design since it leads inevitably to a failure of the core under shear forces. On the other side, having  $t_s/t_f < 1$  leads to systematic wrinkling of the skins and is also not interesting.

#### 3.2. Symmetries

The chevron pattern pattern has three major symmetries which also apply to the sandwich panel unit-cell. Applying results from Section 2.4.3 leads to many simplifications of the constitutive law.

The rotational symmetry of axis  $(S, \hat{e}_3)$ , shown in Figure A.4-a, ensures uncoupling between  $(\underline{N}, \underline{M})$  and  $\underline{R}$ . Figure A.4-b shows the central symmetry with respect to the center point of Face  $ABCD$ :  $R$ . This symmetry uncouples  $\underline{N}$  and  $\underline{M}$  (it is a combination of invariances  $\mathcal{S}$  and  $\mathcal{M}$  from Section 2.4.3). Finally Figure A.4-c shows the symmetry with respect to the  $(B, \hat{e}_1, \hat{e}_3)$  plane. This symmetry enforces orthotropy of the plate:  $(N_{11}, N_{22})$  are uncoupled from  $N_{12}$ ;  $(M_{11}, M_{22})$  are uncoupled from  $M_{12}$  and  $(R_{111}, R_{221}, R_{122})$  are uncoupled from  $(R_{222}, R_{112}, R_{121})$ . Thus, at this stage of the presentation, there are 12 independent generalized shear moduli.

#### 3.3. Implementation

In this section, the most important points concerning the numerical implementation are given.

##### 3.3.1. Modeling the unit-cell with shell elements

Since the facets constituting the unit-cell are slender, it is more relevant to use shell finite elements than 3D finite elements for implementing the auxiliary problems introduced in Section 2.4. This necessitates some adaptations to shell models. A fully detailed justification is provided in Appendix A as well as some technical implementation details. We just recall here that displacement field  $\hat{\underline{u}}$  at nodes is replaced by a plate displacement field  $\hat{\underline{U}}$  and a plate rotation field  $\hat{\underline{\theta}}$ . Moreover, stress field  $\hat{\underline{\sigma}}$  in the elements is replaced by plate generalized stress fields  $(\underline{n}, \underline{m}, \underline{q})$  expressed in the facets' local reference frame.

We choose  $S4R$  quadrangle linear shell elements with reduced integration in ABAQUS. Since the facets are homogeneous it is possible to use Reissner-Mindlin elements which are actually Bending-Gradient elements. A convergence study, not detailed here, was performed and led to a mesh with ten elements per edge.

### 3.3.2. The detailed geometry of the unit-cell

The geometry of the core itself was detailed in Figure A.3. It comprises four tilted parallelogram-shaped faces which vertices are  $A, B, C, D, A', D', A'', B''$  and  $A'''$  (Figure A.5). Moreover, the skins are glued or welded along  $D, C, D'$  (upper skin) and  $A, B, A'$  (lower skin). In order to take into account the skins thickness, the mid-plane of the skins is set with a  $t_s/2$  offset (Figure A.5).

The upper and lower skins vertices are denoted with  $A^\pm, B^\pm, C^\pm, D^\pm, A'^\pm, D'^\pm, A''^\pm, B''^\pm$  and  $A'''^\pm$ . Their coordinates are detailed in Table 2, where:

$$a = a_0 \cos \delta, \quad s = b_0 \cos \alpha, \quad v = b_0 \sin \alpha, \quad t_c = a_0 \sin \delta. \quad (20)$$

Vertex	$A$	$B$	$C$	$D$	$A'$	$D'$	$A''$	$B''$	$A'''$
$x_1$	0	$v$	$a + v$	$a$	0	$a$	$2a$	$2a + v$	$2a$
$x_2$	0	$s$	$s$	0	$2s$	$2s$	0	$s$	$2s$
$x_3$	0	0	$t_c$	$t_c$	0	$t_c$	0	0	0
Vertex	$A^-$	$B^-$	$C^-$	$D^-$	$A'^-$	$D'^-$	$A''^-$	$B''^-$	$A'''^-$
$x_1$	0	$v$	$a + v$	$a$	0	$a$	$2a$	$2a + v$	$2a$
$x_2$	0	$s$	$s$	0	$2s$	$2s$	0	$s$	$2s$
$x_3$	$-\frac{t_s}{2}$								
Vertex	$A^+$	$B^+$	$C^+$	$D^+$	$A'^+$	$D'^+$	$A''^+$	$B''^+$	$A'''^+$
$x_1$	0	$v$	$a + v$	$a$	0	$a$	$2a$	$2a + v$	$2a$
$x_2$	0	$s$	$s$	0	$2s$	$2s$	0	$s$	$2s$
$x_3$	$t_c + \frac{t_s}{2}$								

Table 2: Vertices' coordinates

In order to bind the core and the skins, a rigid kinematic coupling is enforced between skins and core along  $D, C, D'$  for the upper skin:

$$\begin{cases} \hat{\mathbf{U}}^{DCD'} = \hat{\mathbf{U}}^{D^+C^+D'^+} + \hat{\boldsymbol{\theta}}^{D^+C^+D'^+} \times \frac{t_s}{2} \hat{\mathbf{e}}_3 \\ \hat{\boldsymbol{\theta}}^{DCD'} = \hat{\boldsymbol{\theta}}^{D^+C^+D'^+} \end{cases}$$

and along  $A, B, A'$  for the lower skin:

$$\begin{cases} \hat{\mathbf{U}}^{ABA'} = \hat{\mathbf{U}}^{A^+B^+A'^-} + \hat{\boldsymbol{\theta}}^{A^+B^+A'^-} \times \left(-\frac{t_s}{2} \hat{\mathbf{e}}_3\right) \\ \hat{\boldsymbol{\theta}}^{ABA'} = \hat{\boldsymbol{\theta}}^{A^+B^+A'^-} \end{cases}$$

Finally, periodicity conditions must be applied:  $A^\pm D^\pm A''^\pm$  matches  $A'^\pm D'^\pm A'''^\pm$ ,  $A^\pm B^\pm A'^\pm$  matches  $A''^\pm B''^\pm A'''^\pm$  and  $ADA''$  matches  $A'D'A'''$  (Figure A.5 and Appendix A).

## 4. Results

### 4.1. Kirchhoff-Love homogenization

In Figure A.6 and Figure A.7 are plotted the deformed unit-cell under Kirchhoff-Love unit strain loads. The facets thickness is  $0.1 \text{ mm}$ , the skins thickness is  $1 \text{ mm}$  and the shape ratio is,  $a_0/b_0 = 1.2$ . The original

geometry is given by a wireframe and the contour plot displays Von Mises stress. One can clearly identify the average strains related to  $\underline{\epsilon}$  and  $\underline{\chi}$  enforced overall on the unit-cell. When computing the Kirchhoff-Love stiffness tensors, expected uncouplings were obtained.

The main observation is that for both membrane and curvature loadings, most of the stress is concentrated in the skins and the core is almost not stressed. This confirms the classical assumption in sandwich panel theory (SPT) that the core does not affect the bending stiffness. Under this assumption, one can derive the commonly used Kirchhoff-Love stiffness, taking only the skins into account:

$$\left( \underset{\approx}{\mathbf{A}}^{\text{SPT}}, \underset{\approx}{\mathbf{D}}^{\text{SPT}} \right) = \left( h - t_c, \frac{h^3 - t_c^3}{12} \right) \underset{\approx}{\mathbf{c}}^m \quad (21)$$

where  $\underset{\approx}{\mathbf{c}}^m$  is the plane-stress stiffness tensor of the constitutive material of the skins. In Figure A.8 is plotted the relative difference between  $D_{1111}^{BG}$  and  $D_{1111}^{\text{SPT}}$  versus the contrast ratio  $t_s/t_f$  for several facets thicknesses. Since all curves seem collapse on a master curve, the contrast ratio appears as a good parameter for quantifying the error in sandwich panel theory. Moreover, for contrast ratio larger than 10,  $D_{1111}^{\text{SPT}}$  gives a very good approximation of the stiffness derived with the homogenization scheme (this was also observed with all components of  $\underset{\approx}{\mathbf{A}}$  and  $\underset{\approx}{\mathbf{D}}$ ).

#### 4.2. Bending-Gradient homogenization

The distance between Bending-Gradient and Reissner-Mindlin theories  $\Delta^{RM/BG}$  is plotted in Figure A.9 versus the contrast ratio for several facets' thickness. The distance is globally decreasing with the contrast ratio and when  $t_s = 2t_f$  it is already smaller than 2%. For contrast ratios greater than 10, the distance is very small (2‰) and becomes steady with respect to the contrast ratio. Clearly, the Bending-Gradient is turned into a Reissner-Mindlin model, especially for high contrast ratios. This means that we only need to consider shear forces  $Q_\alpha$  as macroscopic load and not all of the six components of  $R_{\alpha\beta\gamma}$ . Moreover, there are only two shear forces stiffness moduli to be derived (orthotropy). The constitutive equation becomes:

$$\begin{pmatrix} Q_1 \\ Q_2 \end{pmatrix} = \begin{pmatrix} F_{11} & 0 \\ 0 & F_{22} \end{pmatrix} \begin{pmatrix} \gamma_1 \\ \gamma_2 \end{pmatrix} \quad (22)$$

where  $\underline{\gamma}$  is Reissner-Mindlin shear strain and  $\underline{\mathbf{F}} = \left( \frac{2}{3} \underline{\mathbf{i}} \cdot \underline{\mathbf{i}} : \underline{\mathbf{f}} : \frac{2}{3} \underline{\mathbf{i}} \cdot \underline{\mathbf{i}} \right)^{-1}$  is Reissner-Mindlin conventional stiffness. This simplification into a Reissner-Mindlin model is generalized to any sandwich panel under a contrast assumption between the core and the skins stiffness in Lebée and Sab (2011c).

In Figure A.10 are plotted the deformed unit-cell under shear force unit loads. The overall deformation of the unit-cell looks like uniform shear strain as expected with sandwich panels and one can easily notice the in-plane relative displacement of the skins. The core is more stressed than the skins and the fields in the core are similar to those derived in Lebée and Sab (2010b).

Finally, whereas in Direction 2 the skins remain planar under  $Q_2$  loading, in Direction 1 the skins are clearly distorted (Figure A.11). The out-of-plane displacement of the skin is about 1/3 of the skins relative displacement. This explains the gap between bounds in this direction and affects critically the actual shear forces stiffness.

In Figures A.12 and A.13, the shear forces stiffness moduli are plotted in each direction versus the shape ratio  $a_0/b_0$ . They are normalized with Voigt upper bound for shear forces stiffness

$$F_{\alpha\beta}^V = \rho A_s G_m \quad (23)$$

where

$$\rho = \frac{t_f}{a} \sqrt{1 + \tan^2 \alpha + \cot^2 \delta} \quad (24)$$

is the volume fraction of material in the core,  $G_m$  is the shear modulus of the constitutive material and

$$A_s = t_c \left( \frac{2(h^3 - t_c^3)}{3t_c(h^2 - t_c^2)} \right)^2 \quad (25)$$

is the shear area suggested by Kelsey et al. (1958). The bounds from Kelsey et al. (1958) derived with finite elements in Lebée and Sab (2010b) are also recalled.

The facets thickness is set to  $t_f = 0.1\text{ mm}$  and several skins thicknesses are investigated. The upper bound from Kelsey et al. (1958) is never violated whereas the lower bound is when the contrast ratio is rather low. Actually, in Lebée and Sab (2011c), it is demonstrated that the lower bound from Kelsey et al. (1958) is not strictly justified because it does not take properly into account the contribution of the skins to the shear forces stiffness. As already pointed out with the bounds in Lebée and Sab (2010b), the shape ratio has a strong influence on the actual shear forces stiffness in both directions.

It is noticeable that the moduli derived with the Bending-Gradient homogenization scheme cover all the range between the bounds from Kelsey et al. (1958) when varying the skins thickness. Thus we conclude that these bounds cannot be improved without a detailed analysis of the interaction between the skins and the core. Furthermore, the upper bound is reached only for extremely high contrast ratio. This contradicts the common practice of choosing only the upper bound for designing sandwich panels.

Finally, in both directions, the thicker the skins are, the closer to the upper bound the shear forces stiffness is. This confirms the interpretation given by Kelsey et al. (1958) for their bounds: the upper bound is relevant for thick skins and the lower one for thin skins. Further analysis of this phenomenon is provided in the discussion of Section 5.

#### 4.3. Comparison with full 3D simulation

In order to validate the Bending-Gradient model, the homogenized solution derived with the Bending-Gradient homogenization scheme is compared with a full 3D simulation of the sandwich panel under the cylindrical bending configuration from Pagano (1969). The sandwich panel is simply supported in  $x_1 = 0, L$  and infinite in  $x_2$  direction. It is transversely loaded with a sine distribution:  $p_3 = p_0 \sin \frac{\pi x_1}{L}$ .

The Bending-Gradient/Reissner-Mindlin solution for this configuration was derived in Lebée and Sab (2011b). Orthotropic uncouplings lead directly to the deflection:

$$U_3(x_1) = p_0 \left( \frac{L}{\pi} \right)^4 \left( \frac{1}{D_{1111}} + \frac{\pi^2}{L^2 F_{11}} \right) \sin \frac{\pi x_1}{L} \quad (26)$$

where  $L$  is the span,  $D_{1111}$  and  $F_{11}$  are the stiffness moduli derived from the homogenization scheme.

An illustration of the full 3D simulation is given in Figure A.14. The unit-cell geometry is the same as in Figure A.6. The span covers 18 cells:  $L = 308\text{ mm} \simeq 10h$ . Simple supports are modeled with rigid rolls which diameter is  $3t_c$ . Actually these boundary conditions are much closer to the reality than those implicitly defined in plate models. Periodicity conditions in Direction 2 are enforced along the edge of the 9.5 cells strip in Figure A.14. At mid-span, the rotational symmetry  $\mathcal{S}$  with respect to a vertical axis is used to restrict the analysis to half a span. This symmetry was detailed in Section 3.2. The same elements as for the homogenization scheme are used. Because of the supporting rolls, contact with the sandwich panel is taken into account. The sandwich panel is loaded on the lower and upper skins with  $\hat{\mathbf{T}}^\pm = \frac{p_3}{2} \hat{\mathbf{e}}_3$  where  $p_3 = -p_0 \sin \frac{\pi x_1}{L}$ . The loading  $p_0$  is chosen small enough so that we remain in the linear elastic range.

On Figure A.14, the skins distortion is clearly visible. In order to compare with the prediction from the Bending-Gradient model, the plate deflection from the 3D simulation is derived as the average between the upper skin and the lower skin deflections. Moreover, this deflection is averaged in the  $x_2$  direction. Two arbitrary facet thicknesses are investigated:  $t_f = 0.1\text{ mm}$  and  $t_f = 2\text{ mm}$  as well as two skin thicknesses:  $t_s = 5\text{ mm}$  and  $t_s = 1\text{ mm}$ . On Figures A.15 to A.18 are plotted the deflection curves. For each sandwich panel configuration, four deflection curves are plotted: the full simulation and the Bending-Gradient gradient prediction, but also the deflections using only the bounds from Kelsey et al. (1958) for the shear forces stiffness. The deflection is normalized with the Kirchhoff-Love deflection of the plate ( $F_{11} = \infty$ ).

For all configurations, there is a very good agreement between the Bending-Gradient predictions and the 3D solution. Because of the different supports between the Bending-Gradient solution and the 3D simulation, it is not possible to give a quantitative comparison of deflections. For instance, in Figure A.16, the skins own flexural stiffness close to supporting rolls generates an offset in the deflection of the 3D model. The qualitative comparison is nevertheless convincing. Furthermore, the contribution of transverse shear to

the deflection is clearly non-negligible and the gap between the deflections based on the bounds from Kelsey et al. (1958) illustrates the need of accurate estimate of shear forces stiffness.

Finally, 3-point bending was also performed in order to test more realistic loadings for sandwich panels. The results are very similar to those presented here; provided the thickness of the skins is not too large compared to the overall thickness of the sandwich panel ( $t_s/h < 1/10$ ). Otherwise, the skins own flexion must be taken into account with second moments in order to predict accurately the deflection.

## 5. Discussion on shear forces stiffness

The application of the Bending-Gradient homogenization scheme in Section 4.2 brought out a skin distortion phenomenon when the sandwich panel including the chevron pattern is loaded in Direction 1. A strong influence on the shear forces stiffness is then observed. Actually, the interaction between the skins and the core has already been pointed out with honeycomb and more critically with corrugated cardboard (Nordstrand and Carlsson, 1997). In this section we first recall the existing work already done with honeycomb in order to identify the specificities of the chevron pattern. Then the importance of the distortion effect in sandwich panels assessment is finally discussed.

### 5.1. The case of honeycomb structures

In the case of a sandwich panel including honeycomb loaded with shear forces, the interaction between the skins and the core is mainly caused by an incompatibility between the overall transverse shear strain field in the core and the skins own stiffness. This interaction is driven by two phenomena: a trade-off between skin and core stiffnesses and a boundary layer effect.

The incompatibility itself is caused by the non-uniform shear strain in the core far from the skins. Especially there is out-of-plane warping of the honeycomb core. Close to the skins, this warping is restrained which generates local flexion in the skins. Since warping involves in-plane shearing of the honeycomb facets, this phenomenon is driven by a trade-off between the skins flexural stiffness and the facets membrane stiffness.

This incompatibility phenomenon is a boundary layer and remains close to the skins because of a slenderness effect (named also thickness effect by Becker (1998)). In many sandwich panels including honeycomb, the in-plane size  $l$  of the unit-cell is rather small compared to the core thickness  $t_c$  (Figure A.19). Thus, when  $t_c/l$  is large enough and assuming the skins fully rigid, the unit-cell can be considered as a beam doubly clamped to the skins. The strain incompatibility caused by clamping remains localized close to the skins. This phenomenon is directly driven by the aspect ratio of the unit-cell  $t_c/l$ . A model illustrating such boundary effects caused by strains incompatibility on the edge is suggested in Lebée and Sab (2010a).

This boundary layer effect was pointed out by Grediac (1993) when applying the unit displacement method from Kelsey et al. (1958) with finite elements. Grediac (1993) demonstrated the influence of the unit-cell aspect ratio on the upper bound for shear forces stiffness. When  $l/t_c$  decreases, the finite elements upper bound computed by Grediac (1993) decreases and becomes close to the lower bound because the incompatibility remains close to the skins. His work was followed by analytical approaches from Becker (1998, 2000) and Chen and Davalos (2005) where the strain incompatibility is treated as a boundary effect. However all these works assume fully rigid skins. Thus the trade-off between the skins stiffness and the facets membrane stiffness was not pointed out.

In order to take into account the full interaction between skins and core under transverse shear loading, Shi and Tong (1995) suggested to apply a uniform transverse shear strain on average in the core (as done in periodic homogenization schemes) to which are welded the skins. This enabled them to bring out both the unit-cell aspect ratio and the skins own flexural stiffness influence on the actual shear forces stiffness of honeycombs. Their approach was applied to several honeycomb geometries by Hohe (2003) who calls it the direct homogenization method.

Even if this approach is based on a relevant analysis of the mechanical behavior of sandwich panels under shear forces, its main limitation is that it is valid only for thin skins. When the skins become thick, they carry a non-negligible part of shear forces and must be taken into account in the estimation of shear

forces stiffness. Actually there is an inherent contradiction when assuming thin skins and trying to assess the influence of their thickness on the shear forces stiffness. The Bending-Gradient homogenization scheme is not limited by the skins thickness.

### 5.2. The case of chevron pattern

Like with honeycomb, there is a shape ratio  $a_0/b_0$  for the chevron pattern. As indicated in Section 4.2 this shape ratio has a strong influence on the shear forces stiffness. However, it is difficult to relate  $a_0/b_0$  to some scale separation or slenderness effect. Moreover in practical case  $a_0/b_0 \in [0.25, 1.5]$  (Zakirov et al., 2006) thus it would be irrelevant to look for limit cases and a boundary layer effect.

There remains the skins distortion effect. Two combined phenomenon could explain the shear forces stiffness variations.

First, in Lebée and Sab (2010b) we indicated that facets mostly behave as membranes. Hence exactly as for the honeycomb, the shear forces stiffness is mostly driven by the facets membrane stiffness which compete with the skins own flexural stiffness. In the present case, this trade-off is proportional to the ratio between the skins flexural stiffness and the facets membrane stiffness:  $t_s/(t_f h^2)^{1/3}$  which we call the skins relative flexural stiffness (an equivalent parameter was suggested by Shi and Tong (1995)).

Second, since the facets are clamped on the skins, there can be local flexion in the facets or in the skins. Thus, when the skins are thin and the facets thick enough, there could be a competition between flexion in the skins or flexion in the facets. This phenomenon is driven by a trade-off between facets and skins flexural stiffness. In the present case, this trade-off is proportional to the cube of the contrast ratio  $t_s/t_f$ .

In order to investigate the last two phenomena, the shape ratio is chosen as  $a_0/b_0 = 1$  in the following.

In Figure A.20 the shear forces stiffness in Direction 1,  $F_{11}$  is plotted versus the contrast ratio  $t_s/t_f$  for several facets thicknesses. The bounds from Kelsey et al. (1958) derived with finite elements in (Lebée and Sab, 2010b) are recalled. Globally,  $F_{11}$  increases with the contrast ratio and complies with the upper bound from Kelsey et al. (1958). For low contrasts ( $< 2$ ), the lower bound from Kelsey et al. (1958) is sometimes violated. Moreover the shear forces stiffness is only function of the contrast ratio  $t_s/t_f$  in this range: it does not depend on the facets slenderness  $t_f/h$  (all curves are superposed). Hence, with thin skins ( $t_s/t_f < 2$ ), it is the competition between flexion in the core or in the skins which drives the stiffness. Large skins deformation were observed with finite elements computations. For contrast ratio larger than 2, a shift between the lower bound and the upper bound occurs. This shift depends on both the contrast ratio and the facets thickness. When the shift occurs, no more skins distortion is observed in finite elements computations.

In Figure A.21 the shear forces stiffness in Direction 1 is plotted versus the skins relative flexural stiffness  $t_s/(t_f h^2)^{1/3}$  for several facet thicknesses. All shifts occur for the same value of this parameter ( $t_s/(t_f h^2)^{1/3} \simeq 0.4$ ). This justifies the interpretation of the skins distortion as a trade-off between skins flexural stiffness and facets membrane stiffness suggested above.

In Direction 2, the shear forces stiffness is only function of the contrast ratio  $t_s/t_f$  and does not depend on the facets relative thickness (Figure A.22). Contrary to Direction 1, there is no clear shift between the upper and the lower bound. Very small out-of-plane skins deformations were observed in finite elements results. Here, it is only the competition between flexion in the core or in the skins which drives the stiffness.

### 5.3. Consequence of skins distortion

One can wonder if the distortion effect has to be taken into account with conventional sandwich panel applications including the chevron pattern since shear effects are usually second order effects.

Here is a first answer in the linear elastic domain. Let us consider such a sandwich panel under the cylindrical bending introduced in Section 4.3. The mid-span deflection (Equation (26)) can be rewritten as:

$$U_3 = U^{KL} \left( 1 + \left( \frac{L^*}{L} \right)^2 \right)$$

where  $U^{KL} = \frac{p_0}{D_{1111}} \left(\frac{L}{\pi}\right)^4$  is Kirchhoff-Love deflection,  $L^* = \pi \sqrt{\frac{D_{1111}}{F_{11}}}$  is a characteristic length to which the span must be compared and  $\left(\frac{L^*}{L}\right)^2$  is the shear forces contribution to the deflection. When  $L \gg L^*$  the contribution is negligible. For a homogeneous and isotropic plate  $L^* \simeq h$ . In Figure A.23  $L^*/h$  is plotted as a function of the contrast ratio. This leads to three remarks.

First, we have  $L^*/h \gg 1$ . Having  $L^*/h \ll 1$  would mean that the plate behavior is completely dominated by flexion. Actually, in such a case, one can wonder the meaning of a shear effect which is negligible compared to the unit-cell size and the homogenization approach becomes inconsistent.

Second, in the present case, the shear deflection cannot be neglected. For instance, in standard sandwich panel applications, the slenderness ratios  $L/h$  are seldom larger than 40. In this extreme case, with a contrast ratio of  $t_s/t_f = 10$ , we have  $L^*/h \simeq 10$  and already  $(L^*/L)^2 = 6.25\%$ .

Third, the skins distortion occurs exactly in the standard range for contrast ratio. We conclude that this phenomenon has a central role when one wants to predict accurately sandwich panels deflection including the chevron pattern.

The non-linear elasticity is out of the scope of this work. However, let us recall that the failure of sandwich panels is mainly due to buckling. The work from Petras and Sutcliffe (1999) is a good illustration for an analytical and experimental approach of honeycomb sandwich panels failure map. It is also very interesting to consider the work from Pahr and Rammerstorfer (2006) and Rammerstorfer et al. (2006) were the numerous failure modes are numerically investigated. In many of these failure, the out-of-plane displacement of the skins is involved. Thus, in the case of the chevron pattern, the skins distortion might really affect the bifurcation point.

## 6. Conclusion

In this work, the Bending-Gradient plate theory was extended to periodic plates through a homogenization scheme. Even if this approach might look more complex than classical tools for sandwich panels, it is not limited by any assumption or symmetries. It enables the derivation of the actual stress in the unit-cell generated by macroscopic loads in addition to the macroscopic deflection. Furthermore, it is possible to perform the homogenization of a unit-cell constituted of structural elements and not necessarily 3D continuum FE.

Once applied to a sandwich panel including the chevron pattern, the prediction given by the Bending-Gradient theory was validated by comparing with a full simulation of the sandwich panel. Concerning membrane and flexural moduli, the classical formula from the sandwich panel theory appears to be a good approximation of the actual moduli. When applying the shear auxiliary problem, it turned out that the Bending-Gradient is turned into a Reissner-Mindlin model especially for large contrast ratios. This simplification is extended to all type of sandwich panels provided a contrast assumption in Lebée and Sab (2011c). Moreover, a skin distortion phenomenon was pointed out. This interaction between skins and core is generally ignored, but in the present case it has a critical effect on the shear forces stiffness even in very conventional designs. This phenomenon was explained by a competition between the skins own flexural stiffness and the core membrane stiffness.

Since the Bending-Gradient homogenization scheme gives the local stress in the plate generated by shear forces, it becomes possible to estimate the strength of the sandwich panel. Actually, the present study illustrates clearly that an accurate knowledge of the loading related to shear forces is critical for deriving the actual buckling load. This comes in addition to the observation from Baranger et al. (2010b) that small geometrical defects have strong influence on the stiffness and the strength of folded cores. Incorporating these defects in the Bending-Gradient homogenization scheme is easy and might finally lead to a noticeable improvement of the modeling of sandwich panels.

## References

ABAQUS, 2007. ABAQUS/Standard user's manual, version 6.7.

- Baranger, E., Cluzel, C., Guidault, P.-A., 2010a. Modelling of the behaviour of aramid folded cores up to global crushing. Strain, no-no.  
URL <http://dx.doi.org/10.1111/j.1475-1305.2010.00753.x>
- Baranger, E., Guidault, P.-A., Cluzel, C., 2010b. Numerical modeling of the geometrical defects of an origami-like sandwich core. Composite Structures In Press, Accepted Manuscript, –.  
URL <http://www.sciencedirect.com/science/article/B6TWP-52MJ8WR-3/2/1c040e8a764abfe5ba437c2e003a9ced>
- Basily, B., Elsayed, A., 2004a. A continuous folding process for sheet materials. International Journal of Materials and Product technology 21, 217–238.
- Basily, B., Elsayed, A., 01 2007. Technology for continuous folding of sheet materials into a honeycomb-like configuration.
- Basily, B., Elsayed, E., 2004b. Dynamic axial crushing of multi-layer core structures of folded chevron patterns. International Journal of Materials and Product technology 21, 169–185.
- Becker, W., 1998. The in-plane stiffnesses of a honeycomb core including the thickness effect. Archive of Applied Mechanics 68 (5), 334–341.  
URL <http://dx.doi.org/10.1007/s004190050169>
- Becker, W., Jan. 2000. Closed-form analysis of the thickness effect of regular honeycomb core material. Composite Structures 48 (1-3), 67–70.  
URL <http://www.sciencedirect.com/science/article/pii/S0263822399000744>
- Caillerie, D., 1984. Thin elastic and periodic plates. Mathematical Methods in the Applied Sciences 6 (2), 159 – 191.
- Cecchi, A., Sab, K., Sep. 2007. A homogenized reissner-mindlin model for orthotropic periodic plates: Application to brickwork panels. International Journal of Solids and Structures 44 (18-19), 6055–6079.  
URL <http://www.sciencedirect.com/science/article/B6VJS-4N1T1VS-1/2/d919620a660bf31984dd2242f004ad11>
- Chen, A., Davalos, J. F., 2005. A solution including skin effect for stiffness and stress field of sandwich honeycomb core. International Journal of Solids and Structures 42 (9-10), 2711 – 2739.  
URL <http://www.sciencedirect.com/science/article/B6VJS-4DR86PM-4/2/8e4e2de69692e3b560e86b40f9fc6abf>
- Fischer, S., Drechsler, K., Kilchert, S., Johnson, A., Dec. 2009. Mechanical tests for foldcore base material properties. Composites Part A: Applied Science and Manufacturing 40 (12), 1941–1952.  
URL <http://www.sciencedirect.com/science/article/B6TWN-4VXTSTK-2/2/a347db537ef46087ea1bd6c6fcec0f0c>
- Forest, S., Pradel, F., Sab, K., Jun. 2001. Asymptotic analysis of heterogeneous cosserat media. International Journal of Solids and Structures 38 (26-27), 4585–4608.  
URL <http://www.sciencedirect.com/science/article/B6VJS-4378T5G-8/2/d687891c92ab7d5f4df37358e067cf3b>
- Gewiss, L. V., 12 1960. Dispositifs pour le faonnage mécanique en continu de structures chevronnées développables.
- Grediac, M., 1993. A finite-element study of the transverse-shear in honeycomb-cores. International Journal of Solids and Structures 30 (13), 1777–1788.
- Heimbs, S., 2009. Virtual testing of sandwich core structures using dynamic finite element simulations. Computational Materials Science 45 (2), 205–216.  
URL <http://www.sciencedirect.com/science/article/B6TWM-4TRR8RD-5/2/c519a73bc682a8a5b5c3e7bb037b4234>
- Heimbs, S., Cichosz, J., Klaus, M., Kilchert, S., Johnson, A., May 2010. Sandwich structures with textile-reinforced composite foldcores under impact loads. Composite Structures 92 (6), 1485–1497.  
URL <http://www.sciencedirect.com/science/article/B6TWP-4XNF467-1/2/9becb70f4e7e28ddf8179475dad75f73>
- Hochfeld, H., 09 1959. Process and machine for pleating pliable materials.
- Hohe, J., Oct. 2003. A direct homogenisation approach for determination of the stiffness matrix for microheterogeneous plates with application to sandwich panels. Composites Part B: Engineering 34 (7), 615–626.  
URL <http://www.sciencedirect.com/science/article/B6TWK-493P79Y-2/2/d275a153fa6e44f51a4ea19a04da4e52>
- Kehrlé, R., 05 2004. Method for the production of a sandwich structure for a sandwich composite.
- Kelsey, S., Gellatly, R. A., Clark, B. W., 1958. The shear modulus of foil honeycomb cores: A theoretical and experimental investigation on cores used in sandwich construction. Aircraft Engineering and Aerospace Technology 30 (10), 294 – 302.
- Kintscher, M., Karger, L., Wetzl, A., Hartung, D., May 2007. Stiffness and failure behaviour of folded sandwich cores under combined transverse shear and compression. Composites Part A: Applied Science and Manufacturing 38 (5), 1288–1295.  
URL <http://www.sciencedirect.com/science/article/B6TWN-4MV71TM-1/2/75a32b5f32913f21a03408927e43d577>
- Kling, D., oct 1997. Doubly periodic flat surfaces in three-space. Ph.D. thesis, Rutgers Univ.
- Kling, D. H., 08 2005. Patterning technology for folded sheet structures.
- Kohn, R. V., Vogelius, M., 1984. A new model for thin plates with rapidly varying thickness. International Journal of Solids and Structures 20 (4), 333–350.  
URL <http://www.sciencedirect.com/science/article/B6VJS-482GMF7-16N/2/3406ad339dbfb4aabfcc6656778f0a77>
- Lebé, A., 2010. Thick periodic plates homogenization, application to sandwich panels including chevron folded core. Ph.D. thesis, Université Paris-Est.  
URL <http://tel.archives-ouvertes.fr/tel-00557754/fr/>
- Lebé, A., Sab, K., Apr. 2010a. A cosserat multiparticle model for periodically layered materials. Mechanics Research Communications 37 (3), 293–297.  
URL <http://www.sciencedirect.com/science/article/B6V48-4Y95TX1-1/2/6e88981818134d425cae268adda40a97>
- Lebé, A., Sab, K., Sep. 2010b. Transverse shear stiffness of a chevron folded core used in sandwich construction. International Journal of Solids and Structures 47 (18-19), 2620–2629.  
URL <http://www.sciencedirect.com/science/article/B6VJS-506RCW3-1/2/70a945e9ed2d9b63a1eb91826f306304>
- Lebé, A., Sab, K., Oct. 2011a. A bending-gradient model for thick plates. part I: Theory. International Journal of Solids and Structures 48 (20), 2878–2888.

- URL <http://www.sciencedirect.com/science/article/pii/S0020768311002162>
- Lebé, A., Sab, K., Oct. 2011b. A bending-gradient model for thick plates, part II: Closed-form solutions for cylindrical bending of laminates. *International Journal of Solids and Structures* 48 (20), 2889–2901.  
URL <http://www.sciencedirect.com/science/article/pii/S0020768311002150>
- Lebé, A., Sab, K., 2011c. Homogenization of cellular sandwich panels. *accepted in Comptes Rendus de Mécanique*.
- Miura, K., 1972. Zeta-core sandwich - its concept and realization. ISAS report 37 (6), 137–164.  
URL <http://ci.nii.ac.jp/naid/110001101664/en/>
- Nguyen, M., Jacombs, S., Thomson, R., Hachenberg, D., Scott, M., Feb. 2005. Simulation of impact on sandwich structures. *Composite Structures* 67 (2), 217–227.  
URL <http://www.sciencedirect.com/science/article/B6TWP-4DTBV6Y-3/2/27b185d6e21e57d1f8cb7b3ed7fd3ac5>
- Nordstrand, T. M., Carlsson, L. A., Feb. 1997. Evaluation of transverse shear stiffness of structural core sandwich plates. *Composite Structures* 37 (2), 145–153.  
URL <http://www.sciencedirect.com/science/article/B6TWP-3SP31DG-D/2/1589025a2ef1ac2598cf7c0db6a1fde4>
- Pagano, N., 1969. Exact solutions for composite laminates in cylindrical bending. *Journal of Composite Materials* 3 (3), 398–411.  
URL <http://jcm.sagepub.com/cgi/content/abstract/3/3/398>
- Pahr, D. H., Rammerstorfer, F. G., Apr. 2006. Buckling of honeycomb sandwiches: Periodic finite element considerations. *CMES-Computer Modeling In Engineering & Sciences* 12 (3), 229–241.
- Petras, A., Sutcliffe, M. P. F., Apr. 1999. Failure mode maps for honeycomb sandwich panels. *Composite Structures* 44 (4), 237–252.  
URL <http://www.sciencedirect.com/science/article/B6TWP-3WWD8Y-3/2/29b075fa63b335896234717a58f4934c>
- Rammerstorfer, F. G., Pahr, D. H., Daxner, T., Vonach, W. K., May 2006. Buckling in thin walled micro and meso structures of lightweight materials and material compounds. *Computational Mechanics* 37 (6), 470–478.  
URL <http://dx.doi.org/10.1007/s00466-005-0731-0>
- Rapp, E., 06 1960. Sandwich-type structural element.
- Shi, G., Tong, P., 1995. Equivalent transverse shear stiffness of honeycomb cores. *International Journal of Solids and Structures* 32 (10), 1383 – 1393.  
URL <http://www.sciencedirect.com/science/article/B6VJS-3YKXJK-49/2/7456379e5ec5788f2eb2514eebccd685>
- Zakirov, I., Alekseyev, K., Mudra, C., 2006. A technique for designing highly-stiffened chevron folded cores. *Russian Aeronautics* 49 (4), 1 – 7.

## Appendix A. Implementation details with plate elements

The homogenization scheme presented in Section 2.4 is valid for 3D continuum mechanics. However, sandwich panels with core made of honeycomb structures or folded material are mostly made of thin facets. In order to limit computational cost, it is more relevant to model the unit-cell of these panels with plate elements: the facets. In this case, the 3D fields in the auxiliary problems  $\mathcal{P}^{LK}$  and  $\mathcal{P}^{BG}$  are replaced by plate generalized stresses, translations and rotations. In this section we provide some adaptation of auxiliary problems to plate fields.

First, boundary conditions in the Kirchhoff-Love auxiliary problem are modified so that it takes into account the rotation field. Then the volume force related to  $\underline{\mathbf{R}}$  is turned into plate loadings.

### Appendix A.1. Boundary conditions in the Kirchhoff-Love auxiliary problem

Introducing the Kirchhoff-Love average displacement,

$$\hat{\underline{\mathbf{U}}}^{KL} = \hat{\underline{\mathbf{e}}} \cdot \hat{\underline{\mathbf{y}}} + y_3 \hat{\underline{\boldsymbol{\chi}}} \cdot \hat{\underline{\mathbf{y}}} - \frac{1}{2} \left( {}^t \hat{\underline{\mathbf{y}}} \cdot \hat{\underline{\boldsymbol{\chi}}} \cdot \hat{\underline{\mathbf{y}}} \right) \hat{\underline{\mathbf{e}}}_3 \quad (\text{A.1})$$

the problem  $\mathcal{P}^{LK}$  Equation (11) can be rewritten in the strictly equivalent form:

$$\mathcal{P}^{LK, bis} \left\{ \begin{array}{l} \hat{\underline{\boldsymbol{\sigma}}}^{KL} \cdot \hat{\underline{\nabla}} = 0 \quad (\text{A.2a}) \\ \hat{\underline{\boldsymbol{\sigma}}}^{KL} = \hat{\underline{\mathbf{C}}} \left( \hat{\underline{\mathbf{y}}} \right) : \hat{\underline{\boldsymbol{\varepsilon}}}^{KL} \quad (\text{A.2b}) \\ \hat{\underline{\boldsymbol{\varepsilon}}}^{KL} = \hat{\underline{\nabla}} \otimes^s \hat{\underline{\mathbf{u}}}^{KL} \quad (\text{A.2c}) \\ \hat{\underline{\mathbf{u}}}^{KL} = \hat{\underline{\mathbf{u}}}^{per} + \hat{\underline{\mathbf{e}}} \cdot \hat{\underline{\mathbf{y}}} + y_3 \hat{\underline{\boldsymbol{\chi}}} \cdot \hat{\underline{\mathbf{y}}} - \frac{1}{2} \left( {}^t \hat{\underline{\mathbf{y}}} \cdot \hat{\underline{\boldsymbol{\chi}}} \cdot \hat{\underline{\mathbf{y}}} \right) \hat{\underline{\mathbf{e}}}_3 \quad \text{on } \partial Y_l \quad (\text{A.2d}) \\ \hat{\underline{\boldsymbol{\sigma}}} \cdot \hat{\underline{\mathbf{e}}}_3 = 0 \quad \text{on free faces } \partial Y_3^\pm \quad (\text{A.2e}) \\ \hat{\underline{\boldsymbol{\sigma}}} \cdot \hat{\underline{\mathbf{n}}} \text{ skew-periodic on lateral boundaries } \partial Y_l \quad (\text{A.2f}) \\ \hat{\underline{\mathbf{u}}}^{per}(y_1, y_2, y_3) \quad (y_1, y_2)\text{-periodic on lateral boundaries } \partial Y_l \quad (\text{A.2g}) \end{array} \right.$$

where loadings  $\underline{\epsilon}$  and  $\underline{\chi}$  appears only on the lateral boundaries of the unit cell. Since the facets are small plates, one have to adapt these boundary conditions to the facets local kinematics: the displacement  $\hat{\underline{U}}$  and the rotation  $\hat{\underline{\theta}}$ .

Rotations are related to the skew-symmetric part of the gradient of the displacement:

$$\hat{\underline{\Theta}} = \frac{1}{2} \left( \hat{\underline{U}} \otimes \hat{\underline{\nabla}} - \hat{\underline{\nabla}} \otimes \hat{\underline{U}} \right)$$

$\hat{\underline{\Theta}}$  is a skew-symmetric matrix and  $\hat{\underline{\theta}}$  is the pseudo-vector derived from  $\hat{\underline{\Theta}}$  (see for instance (Forest et al., 2001)):

$$\forall \hat{\underline{n}}, \quad \hat{\underline{\Theta}} \cdot \hat{\underline{n}} = \hat{\underline{\theta}} \times \hat{\underline{n}}.$$

The skew-symmetric part of  $\hat{\underline{U}}^{KL} \otimes \hat{\underline{\nabla}}$  is :

$$\hat{\underline{\Theta}}^{KL} = \hat{\underline{\Theta}}^{per} + \left( \hat{\underline{\chi}} \cdot \hat{\underline{y}} \right) \otimes \hat{\underline{e}}_3 - \hat{\underline{e}}_3 \otimes \left( \hat{\underline{\chi}} \cdot \hat{\underline{y}} \right) \quad (\text{A.3})$$

and the corresponding rotation pseudo-vector is:

$$\hat{\underline{\theta}}^{KL} = \hat{\underline{\theta}}^{per} + \left( \hat{\underline{e}}_2 \otimes \hat{\underline{e}}_1 - \hat{\underline{e}}_1 \otimes \hat{\underline{e}}_2 \right) \cdot \left( \hat{\underline{\chi}} \cdot \hat{\underline{y}} \right) \quad (\text{A.4})$$

When two edges are matching with periodicity conditions, the difference between displacements is written as:

$$\begin{cases} \Delta \hat{\underline{U}}^{KL} = \hat{\underline{e}} \cdot \Delta \hat{\underline{y}} + y_3 \hat{\underline{\chi}} \cdot \Delta \hat{\underline{y}} - \left( \left( \frac{\hat{\underline{y}}^+ + \hat{\underline{y}}^-}{2} \right) \cdot \hat{\underline{\chi}} \cdot \Delta \hat{\underline{y}} \right) \hat{\underline{e}}_3 \\ \Delta \hat{\underline{\theta}}^{KL} = \left( \hat{\underline{e}}_2 \otimes \hat{\underline{e}}_1 - \hat{\underline{e}}_1 \otimes \hat{\underline{e}}_2 \right) \cdot \left( \hat{\underline{\chi}} \cdot \Delta \hat{\underline{y}} \right) \end{cases} \quad (\text{A.5})$$

where  $\hat{\underline{y}}^-$  and  $\hat{\underline{y}}^+$  are the coordinates of the first and the second corresponding edges and  $\Delta \hat{\underline{y}} = \hat{\underline{y}}^+ - \hat{\underline{y}}^-$ .

The periodicity condition between two matching edges + and - are enforced as:

$$\begin{cases} \hat{\underline{U}}^+ = \hat{\underline{U}}^- + \Delta \hat{\underline{U}}^{KL} \\ \hat{\underline{\theta}}^+ = \hat{\underline{\theta}}^- + \Delta \hat{\underline{\theta}}^{KL} \end{cases} \quad (\text{A.6})$$

These periodicity conditions generalize to any unit-cell configuration those suggested by Hohe (2003) and Pahr and Rammerstorfer (2006) which were restricted to rectangular unit-cell.

In the present case, the unit-cell is constituted of facets which have their own local orientation ( $\dagger$ ) with respect to the main reference frame. Thus  $\hat{\underline{y}}^\dagger$  denote the coordinates in the local reference frame and  $\hat{\underline{y}}^\dagger = \hat{\underline{P}} \cdot \hat{\underline{y}}$ , where  $\hat{\underline{P}}$  is an isometry of the 3D space (Figure A.24).

For a shell element, only rotations with respect to  $\hat{\underline{e}}_1^\dagger$  and  $\hat{\underline{e}}_2^\dagger$  are defined. Thus it is also necessary to restrict the rotation  $\hat{\underline{\theta}}^{KL}$  to its in-plane part in the local reference frame of the facet. The actual rotation offset between matching edges implemented in finite elements code in the main reference frame is finally:

$$\Delta \hat{\underline{\theta}}^{FE} = {}^t \hat{\underline{P}} \cdot \hat{\underline{p}} \cdot \hat{\underline{P}} \cdot \Delta \hat{\underline{\theta}}^{KL}$$

where  $\hat{\underline{p}} = \begin{pmatrix} 1 & 0 & 0 \\ 0 & 1 & 0 \\ 0 & 0 & 0 \end{pmatrix}$  is the in-plane projection operator.

#### Appendix A.2. Localization of Kirchhoff-Love fields

Again, since we are dealing with facets, the local 3D stress  $\hat{\underline{\sigma}}(\hat{\underline{y}})$  is replaced by plate generalized-stress fields  $\hat{\underline{n}}^\dagger(\hat{\underline{y}})$ ,  $\hat{\underline{m}}^\dagger(\hat{\underline{y}})$ ,  $\hat{\underline{q}}^\dagger(\hat{\underline{y}})$  (membrane stress, bending moment and shear forces) which are defined in the local reference frame. Thus, solving the Kirchhoff-Love auxiliary problem A.2 with shell elements for each

individual component of  $\underline{\underline{\boldsymbol{\varepsilon}}}$  and  $\underline{\underline{\boldsymbol{\chi}}}$  leads to the localization of generalized-stress fields  $n_{\alpha\beta\gamma\delta}$ ,  $m_{\alpha\beta\gamma\delta}$  and  $q_{\alpha\beta\gamma}$ . The local generalized-stress field can be reconstructed by linear combination:

$$\begin{cases} \underline{\underline{\boldsymbol{n}}}^{\dagger KL} = \underline{\underline{\boldsymbol{n}}}^{(e)} : \underline{\underline{\boldsymbol{\varepsilon}}} + \underline{\underline{\boldsymbol{n}}}^{(\chi)} : \underline{\underline{\boldsymbol{\chi}}} \\ \underline{\underline{\boldsymbol{m}}}^{\dagger KL} = \underline{\underline{\boldsymbol{m}}}^{(e)} : \underline{\underline{\boldsymbol{\varepsilon}}} + \underline{\underline{\boldsymbol{m}}}^{(\chi)} : \underline{\underline{\boldsymbol{\chi}}} \\ \underline{\underline{\boldsymbol{q}}}^{\dagger KL} = \underline{\underline{\boldsymbol{q}}}^{(e)} : \underline{\underline{\boldsymbol{\varepsilon}}} + \underline{\underline{\boldsymbol{q}}}^{(\chi)} : \underline{\underline{\boldsymbol{\chi}}} \end{cases} \quad (\text{A.7})$$

We recall that  $\underline{\underline{\boldsymbol{\varepsilon}}}$  and  $\underline{\underline{\boldsymbol{\chi}}}$  are considered in the main reference frame whereas the resulting generalized-stresses  $\underline{\underline{\boldsymbol{n}}}^{\dagger KL}$ ,  $\underline{\underline{\boldsymbol{m}}}^{\dagger KL}$  and  $\underline{\underline{\boldsymbol{q}}}^{\dagger KL}$  are written in the local reference frame (two points tensors).

Using the inverted Kirchhoff-Love plate constitutive law, it is possible to write the local generalized-stress field generated by the bending moment:

$$\begin{cases} \underline{\underline{\boldsymbol{n}}}^{\dagger(M)} = \underline{\underline{\boldsymbol{n}}}^{(M)} : \underline{\underline{\boldsymbol{M}}} = \left( \underline{\underline{\boldsymbol{n}}}^{(e)} : \underline{\underline{\boldsymbol{b}}} + \underline{\underline{\boldsymbol{n}}}^{(\chi)} : \underline{\underline{\boldsymbol{d}}} \right) : \underline{\underline{\boldsymbol{M}}} \\ \underline{\underline{\boldsymbol{m}}}^{\dagger(M)} = \underline{\underline{\boldsymbol{m}}}^{(M)} : \underline{\underline{\boldsymbol{M}}} = \left( \underline{\underline{\boldsymbol{m}}}^{(e)} : \underline{\underline{\boldsymbol{b}}} + \underline{\underline{\boldsymbol{m}}}^{(\chi)} : \underline{\underline{\boldsymbol{d}}} \right) : \underline{\underline{\boldsymbol{M}}} \\ \underline{\underline{\boldsymbol{q}}}^{\dagger(M)} = \underline{\underline{\boldsymbol{q}}}^{(M)} : \underline{\underline{\boldsymbol{M}}} = \left( \underline{\underline{\boldsymbol{q}}}^{(e)} : \underline{\underline{\boldsymbol{b}}} + \underline{\underline{\boldsymbol{q}}}^{(\chi)} : \underline{\underline{\boldsymbol{d}}} \right) : \underline{\underline{\boldsymbol{M}}} \end{cases} \quad (\text{A.8})$$

### Appendix A.3. Shear auxiliary problem loading

Finally, the volume force  $\underline{\underline{\boldsymbol{f}}}^{\dagger(R)}$  involved in the shear auxiliary problem  $\mathcal{P}^{BG}$  (Equation (17)) has to be turned into plate loading  $\underline{\underline{\boldsymbol{p}}}^{\dagger(R)}$  and  $\underline{\underline{\boldsymbol{\mu}}}^{\dagger(R)}$  (force and moment per unit surface) in the facet's reference frame. Since it involves different reference frames and respective derivatives, we suggest the following step by step procedure:

Facets are homogeneous plates of thickness  $t$ . Thus the generalized-stress  $(\underline{\underline{\boldsymbol{n}}}^{\dagger(M)}, \underline{\underline{\boldsymbol{m}}}^{\dagger(M)}, \underline{\underline{\boldsymbol{q}}}^{\dagger(M)})$  (Equation (A.8)) is related to the following local 3D stress into the facet:

$$\underline{\underline{\boldsymbol{\hat{\sigma}}}}^{\dagger(M)} = \frac{1}{t} \underline{\underline{\boldsymbol{n}}}^{\dagger(M)} + \frac{12y_3^\dagger}{t^3} \underline{\underline{\boldsymbol{m}}}^{\dagger(M)} + \frac{3}{2t} \left( 1 - \left( \frac{2y_3^\dagger}{t} \right)^2 \right) \left( \underline{\underline{\boldsymbol{q}}}^{\dagger(M)} \otimes \underline{\underline{\boldsymbol{e}}}_3^\dagger + \underline{\underline{\boldsymbol{e}}}_3^\dagger \otimes \underline{\underline{\boldsymbol{q}}}^{\dagger(M)} \right) \quad (\text{A.9})$$

Using transformation formula, the stress field is expressed in the main reference frame:  $\underline{\underline{\boldsymbol{\hat{\sigma}}}}^{\dagger(M)} = \underline{\underline{\boldsymbol{\hat{P}}}} \cdot \underline{\underline{\boldsymbol{\hat{\sigma}}}}^{\dagger(M)} \cdot {}^t \underline{\underline{\boldsymbol{\hat{P}}}}$ . Now it is possible to apply the procedure detailed in Section 2.4.2 for deriving  $\underline{\underline{\boldsymbol{f}}}^{\dagger(R)}$  in the main reference frame. The volume force in the local reference frame is then:  $\underline{\underline{\boldsymbol{f}}}^{\dagger(R)} = {}^t \underline{\underline{\boldsymbol{\hat{P}}}} \cdot \underline{\underline{\boldsymbol{f}}}^{\dagger(M)}$ . Then, we derive the plate loads  $\underline{\underline{\boldsymbol{p}}}^{\dagger(R)}$  and  $\underline{\underline{\boldsymbol{\mu}}}^{\dagger(R)}$  from  $\underline{\underline{\boldsymbol{f}}}^{\dagger(R)}$ :  $\underline{\underline{\boldsymbol{p}}}^{\dagger(R)} = \int_{-\frac{t}{2}}^{\frac{t}{2}} \underline{\underline{\boldsymbol{f}}}^{\dagger(R)} dy_3^\dagger$  and  $\underline{\underline{\boldsymbol{\mu}}}^{\dagger(R)} = \int_{-\frac{t}{2}}^{\frac{t}{2}} y_3^\dagger \underline{\underline{\boldsymbol{f}}}^{\dagger(R)} dy_3^\dagger$

All these steps lead to the following definition of plate loads in the local reference frame generated by a uniform bending gradient in the unit-cell:

$$\begin{cases} p_i^{\dagger(R)} = \left( n_{ij\beta\alpha}^{(M)} + q_{i\beta\alpha}^{(M)} \delta_{j3} + q_{j\beta\alpha}^{(M)} \delta_{i3} \right) P_{\gamma j} R_{\alpha\beta\gamma} \\ \mu_\delta^{\dagger(R)} = m_{\delta\epsilon\beta\alpha}^{(M)} P_{\gamma\epsilon} R_{\alpha\beta\gamma} \end{cases} \quad (\text{A.10})$$

Finite element softwares do not always implement the moment-per-unit-surface loading  $\underline{\underline{\boldsymbol{\mu}}}$  with plate elements. However, it is always possible to load with concentrated  $\underline{\underline{\boldsymbol{F}}}$  force and moments  $\underline{\underline{\boldsymbol{M}}}$  at nodes. The preceding plate loads are then converted into concentrated loads in the main reference frame with:

$$\begin{cases} F_i^{(R)} = S^n P_{ik} \left( n_{kj\beta\alpha}^{(M)} + q_{k\beta\alpha}^{(M)} \delta_{j3} + q_{j\beta\alpha}^{(M)} \delta_{k3} \right) P_{\gamma j} R_{\alpha\beta\gamma} \\ M_i^{(R)} = S^n P_{i\zeta} \left( \delta_{\zeta 2} \delta_{\delta 1} - \delta_{\zeta 1} \delta_{\delta 2} \right) m_{\delta\epsilon\beta\alpha}^{(M)} P_{\gamma\epsilon} R_{\alpha\beta\gamma} \end{cases} \quad (\text{A.11})$$

where  $(\delta_{\zeta 2} \delta_{\delta 1} - \delta_{\zeta 1} \delta_{\delta 2})$  turns  $\underline{\underline{\boldsymbol{\mu}}}$  into a moment pseudo-vector and  $S^n$  is the nodal area.

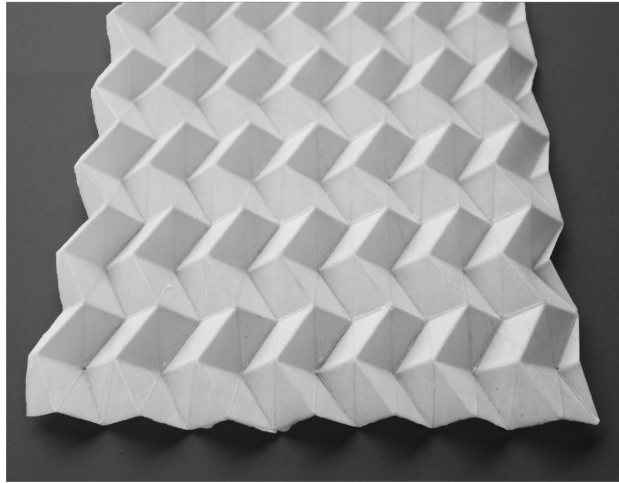


Figure A.1: Chevron folded paper

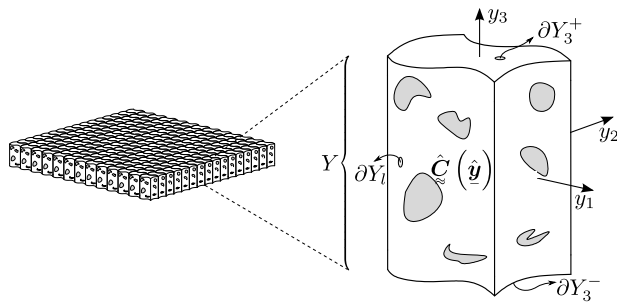


Figure A.2: The plate unit-cell

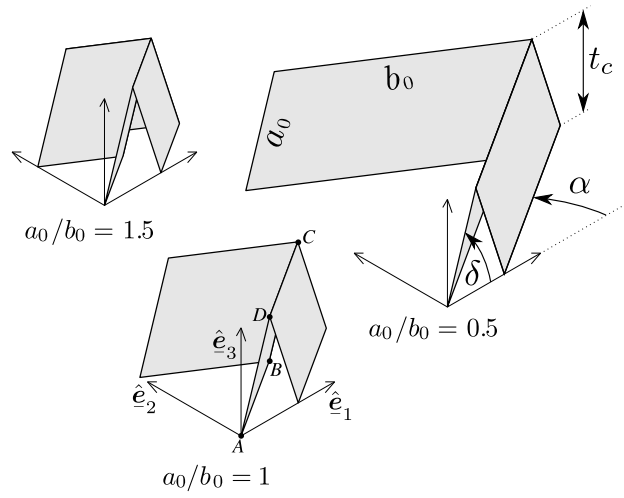


Figure A.3: Chevron pattern investigated configurations.

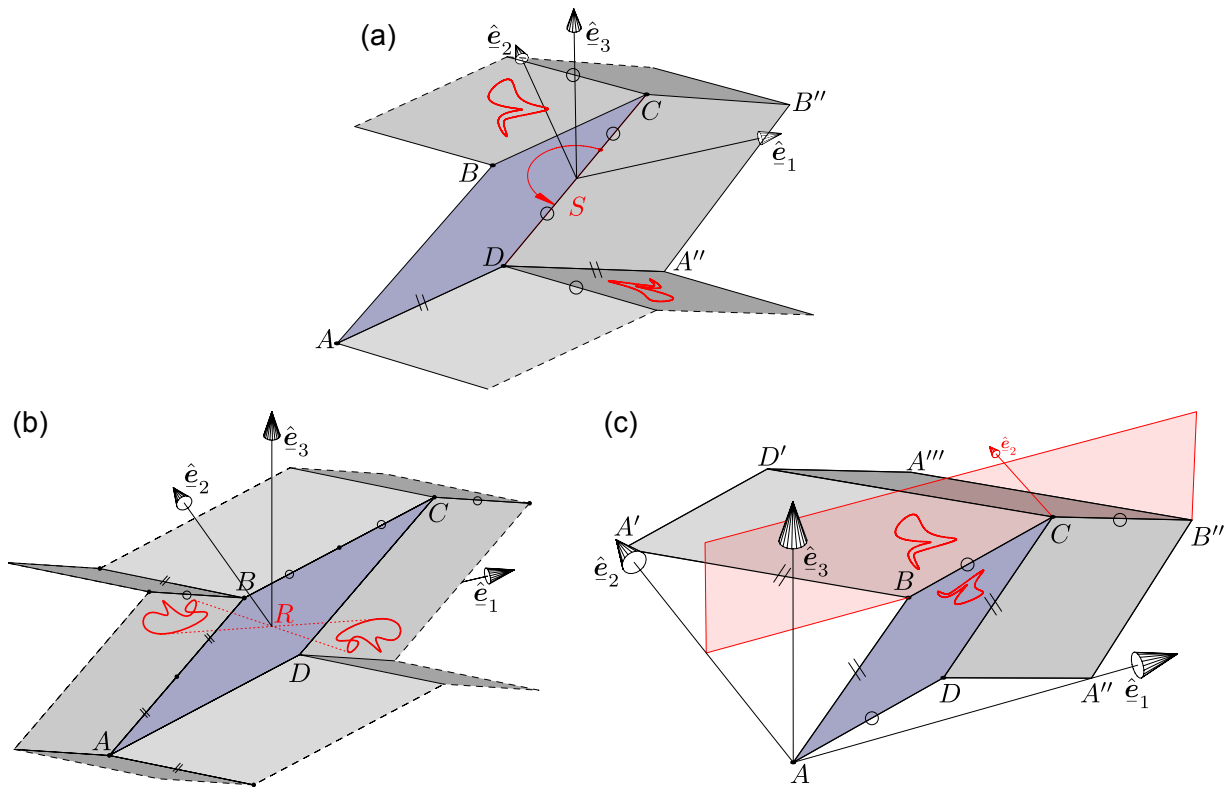


Figure A.4: (a): Rotational symmetry with respect to  $(S, \hat{e}_3)$ . (b): Central symmetry with respect to point  $R$ . (c): Symmetry with respect to  $(B, \hat{e}_1, \hat{e}_3)$  plane.

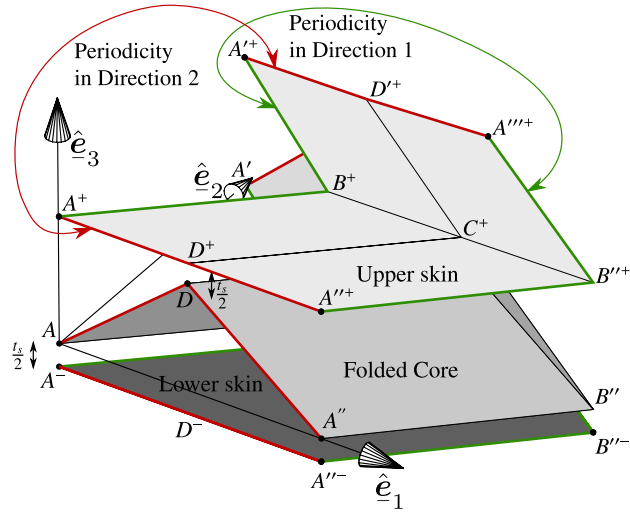


Figure A.5: The sandwich panel unit-cell and periodicity conditions.

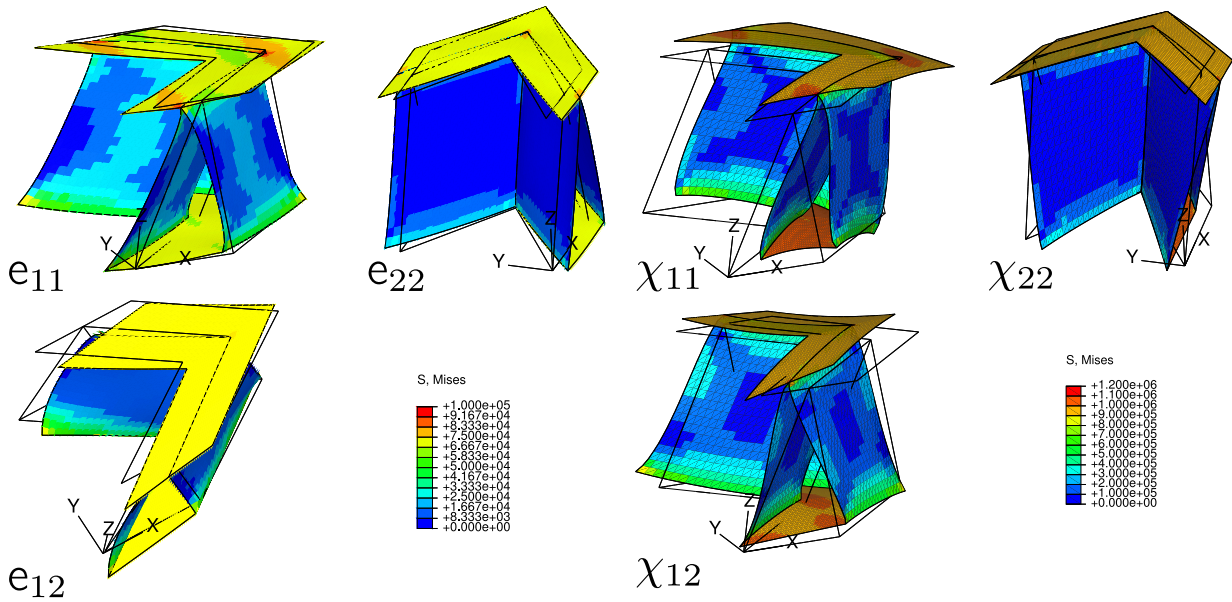


Figure A.6: Deformed unit-cell under Membrane  $\underline{e}$  loading ( $a_0/b_0 = 1.2$ ,  $t_f = 0.1 \text{ mm}$ ,  $t_s = 1 \text{ mm}$ ). The contour plot displays Von Mises stress.

Figure A.7: Deformed unit-cell under Curvature  $\underline{\chi}$  loading ( $a_0/b_0 = 1.2$ ,  $t_f = 0.1 \text{ mm}$ ,  $t_s = 1 \text{ mm}$ ). The contour plot displays Von Mises stress.

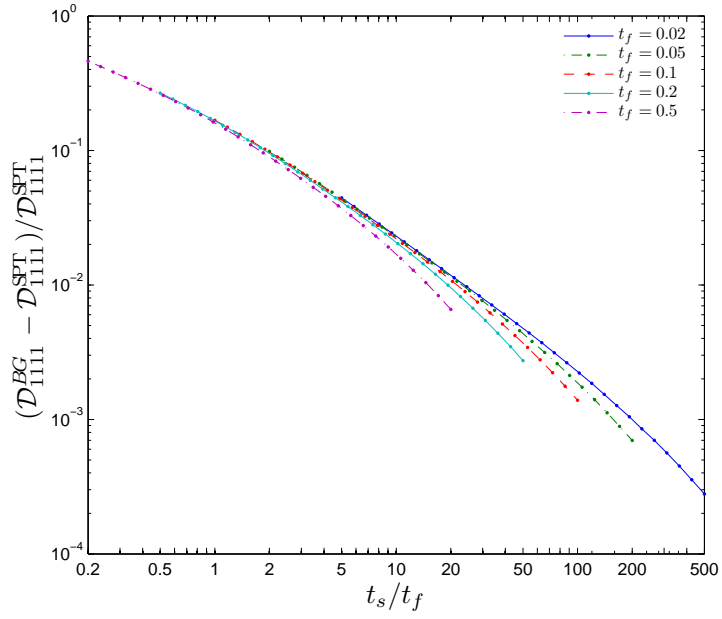


Figure A.8: Relative difference between  $D_{1111}^{BG}$  and  $D_{1111}^{SPT}$  versus the contrast ratio  $t_s/t_f$ .

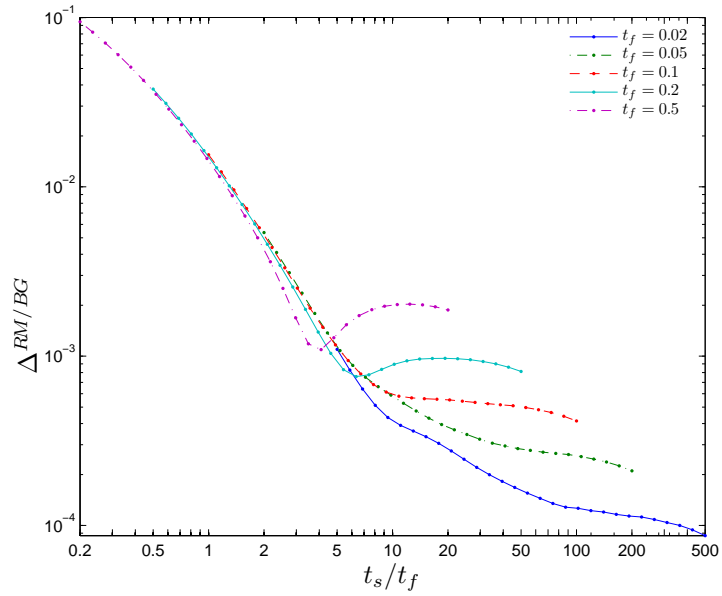


Figure A.9: Distance between Reissner-Mindlin and Bending-Gradient plate model versus the contrast ratio.

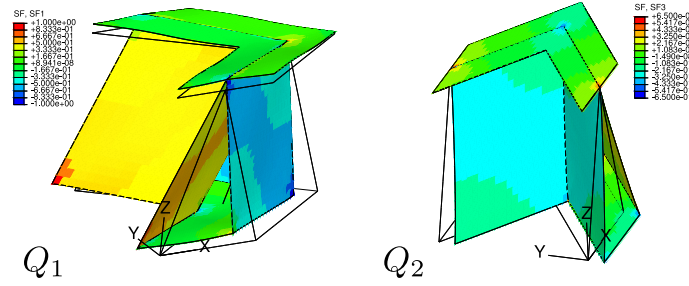


Figure A.10: Deformed unit-cell under shear forces loading ( $a_0/b_0 = 1.2$ ,  $t_f = 0.1 \text{ mm}$ ,  $t_s = 1 \text{ mm}$ ). The contour plot displays local membrane stress  $n_{11}^{(Q)}$  for  $Q_1$  loading and  $n_{12}^{(Q)}$  for  $Q_2$  loading (the local reference frame is such that  $\hat{e}_1^\dagger$  is along  $AD$ ,  $\hat{e}_3^\dagger$  is normal to the facet with  $\hat{e}_3^\dagger \cdot \hat{e}_3 > 0$ ).

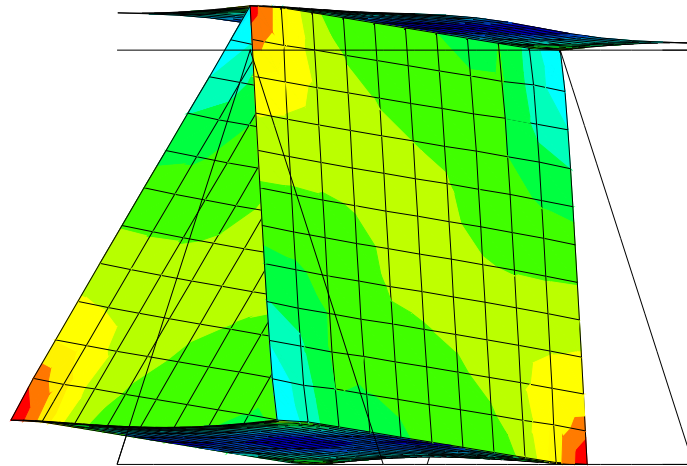


Figure A.11: Deformed unit-cell under  $Q_1$  loading ( $a_0/b_0 = 1.2$ ,  $t_f = 0.1 \text{ mm}$ ,  $t_s = 1 \text{ mm}$ ). View from  $\hat{e}_2$ , Von Mises stress.

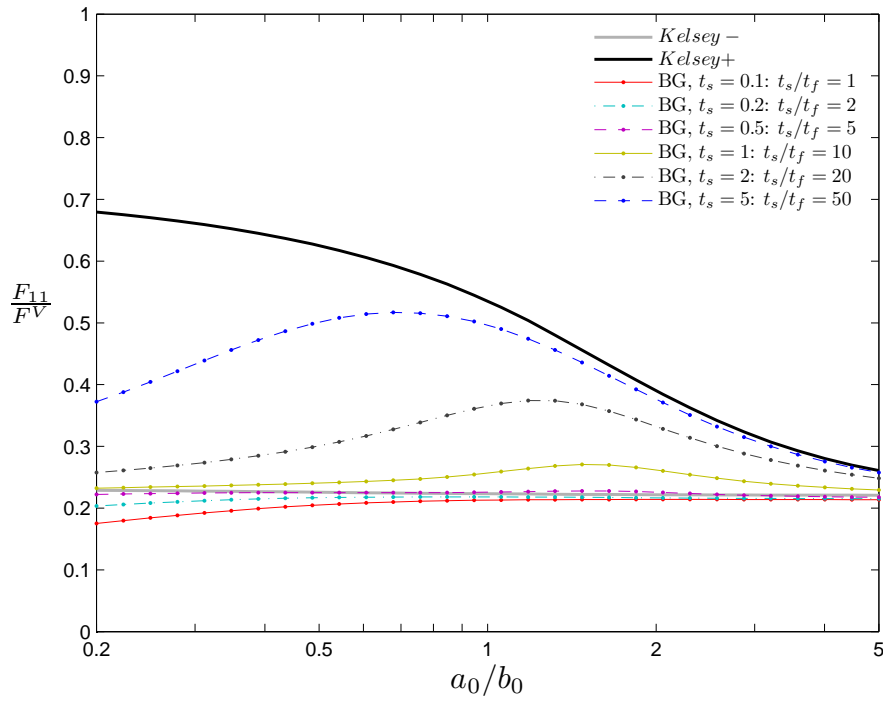


Figure A.12: The normalized shear forces stiffness in Direction 1 vs. the shape ratio for several skin thicknesses ( $t_f = 0.1$ ).

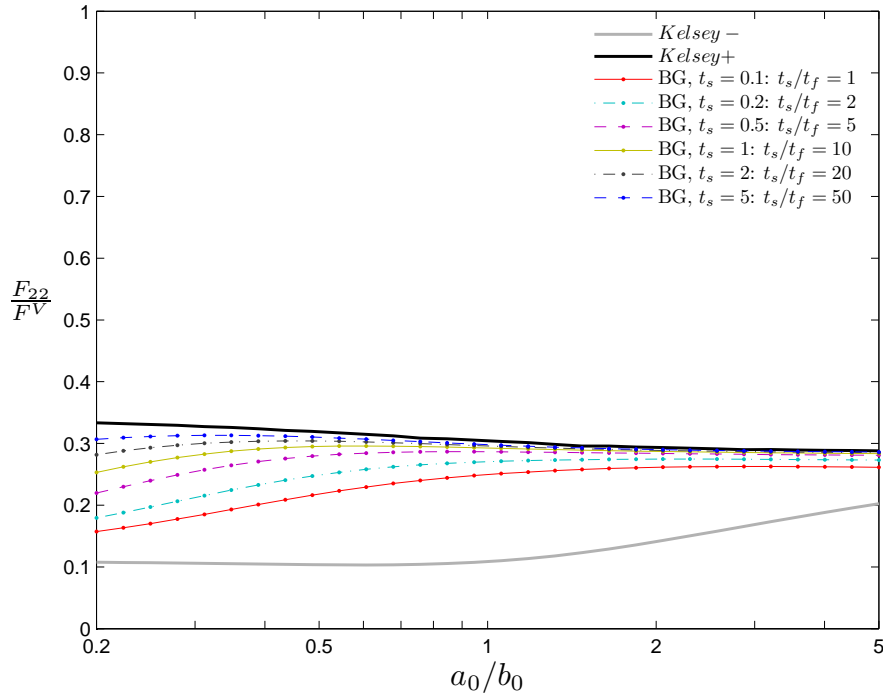


Figure A.13: The normalized shear forces stiffness in Direction 2 vs. the shape ratio for several skin thicknesses ( $t_f = 0.1$ ).

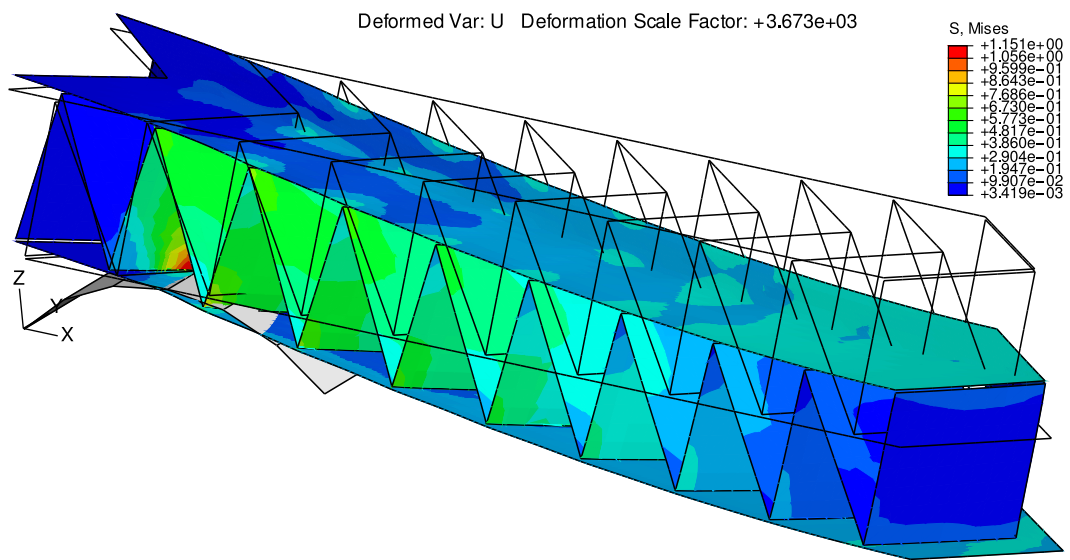


Figure A.14: Overview of the full 3D finite elements cylindrical bending,  $t_s = 1 \text{ mm}$  and  $t_f = 0.1 \text{ mm}$ . Only half span is shown (symmetry).

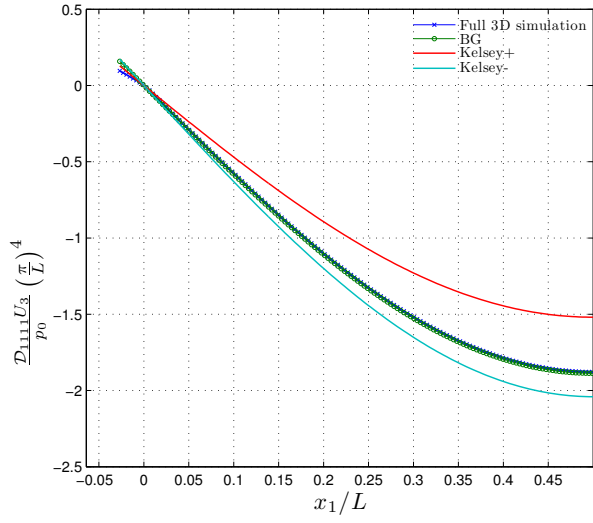


Figure A.15: Deflection along the span for  $t_s = 1 \text{ mm}$  and  $t_f = 0.1 \text{ mm}$ .

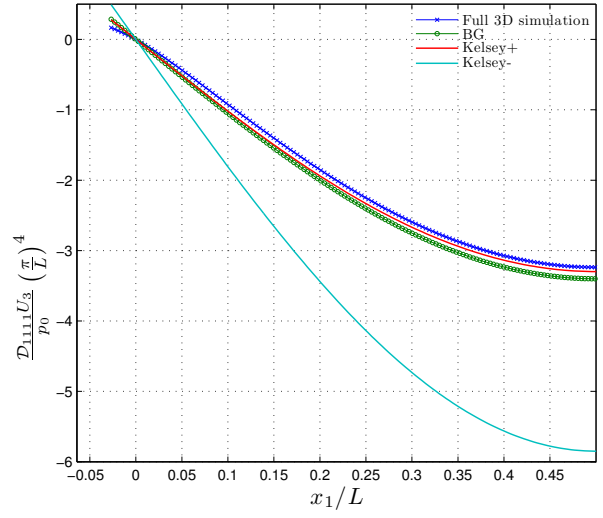


Figure A.16: Deflection along the span for  $t_s = 5 \text{ mm}$  and  $t_f = 0.1 \text{ mm}$ .

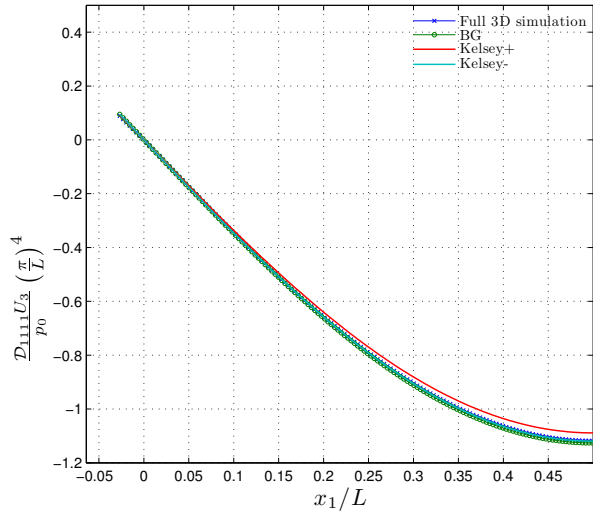


Figure A.17: Deflection along the span for  $t_s = 1 \text{ mm}$  and  $t_f = 2 \text{ mm}$ .

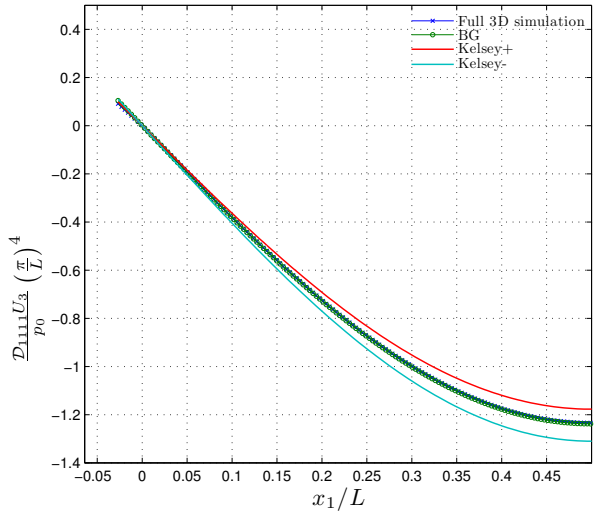


Figure A.18: Deflection along the span for  $t_s = 5 \text{ mm}$  and  $t_f = 2 \text{ mm}$ .

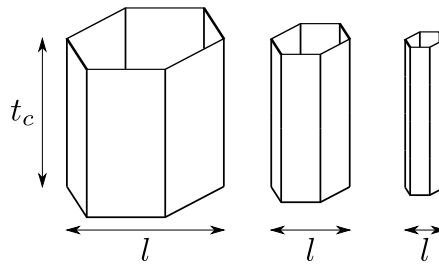


Figure A.19: The honeycomb unit-cell for several aspect ratio.

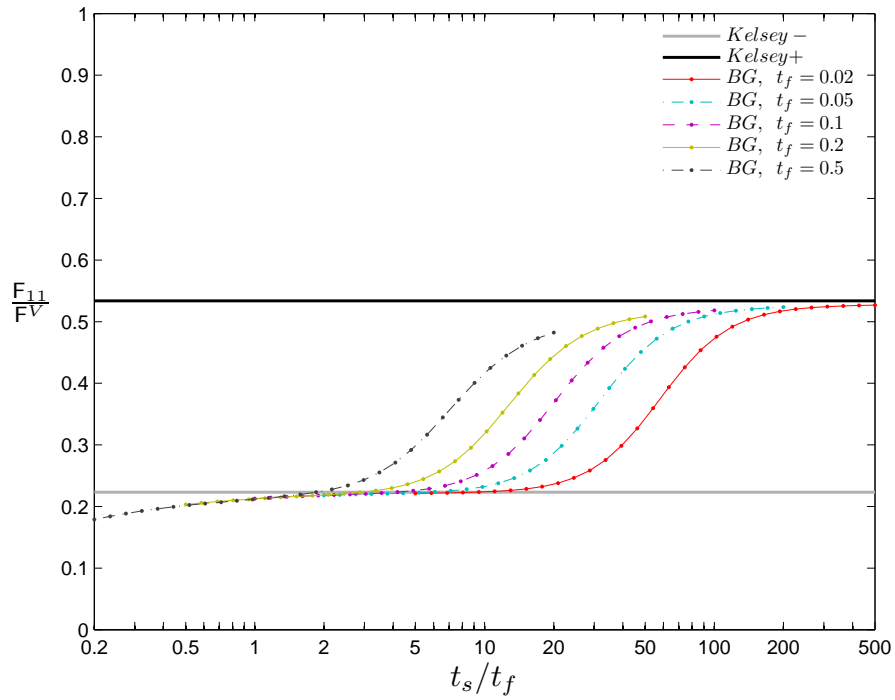


Figure A.20: The normalized shear forces stiffness in Direction 1 vs. the contrast ratio for several facet thicknesses ( $a_0/b_0 = 1$ ).

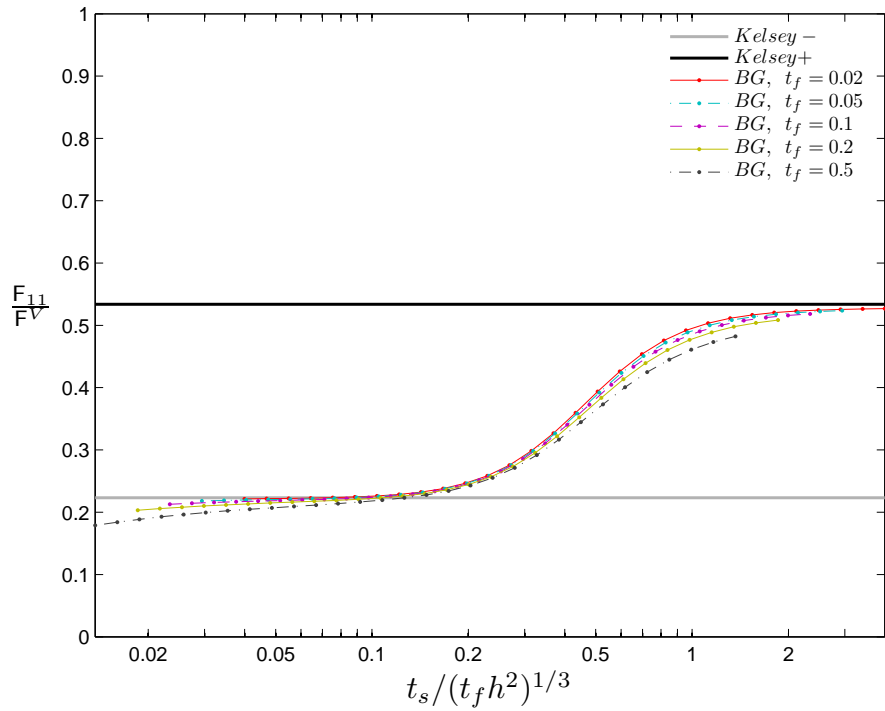


Figure A.21: The normalized shear forces stiffness in Direction 1 vs. skins relative flexural stiffness for several facet thicknesses ( $a_0/b_0 = 1$ ).

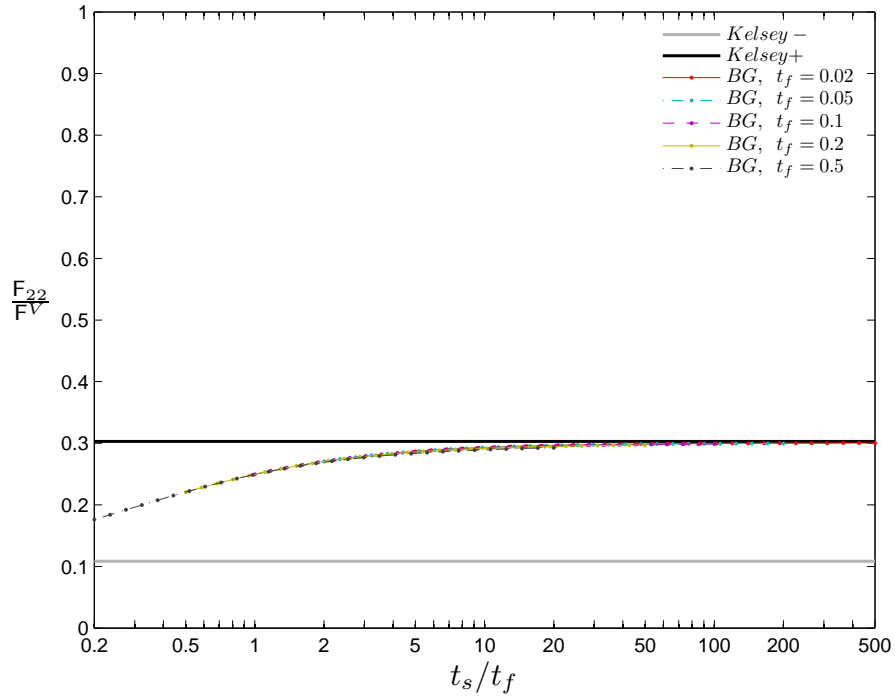


Figure A.22: The normalized shear forces stiffness in Direction 2 vs. the contrast ratio for several facet thicknesses ( $a_0/b_0 = 1$ ).

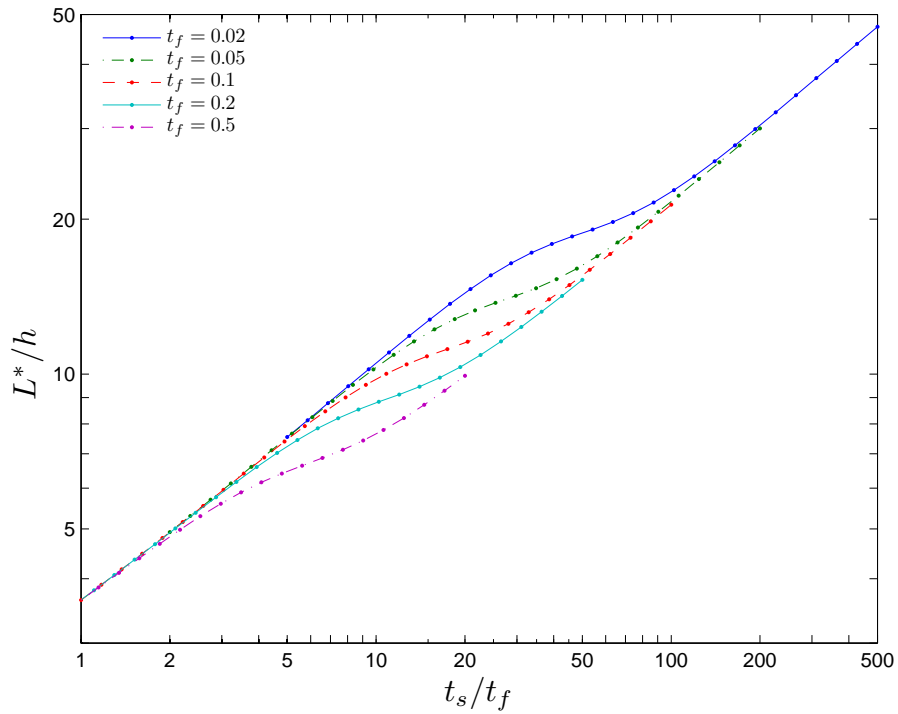


Figure A.23: Shear deflection correction vs. contrast ratio for several facet thicknesses ( $a_0/b_0 = 1$ ).

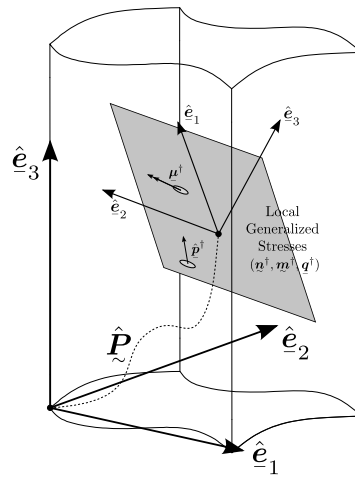


Figure A.24: Local orientation of a facet belonging to the unit-cell.